A SYSTEM ANALYSIS OF THE 13.3 GHz SCATTEROMETER

Job Order 75-415

PREPARED BY

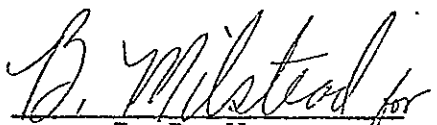

J. R. Wang
Principal Scientist

APPROVED BY

P. J. Walsh, Supervisor
Exploratory Investigations Section

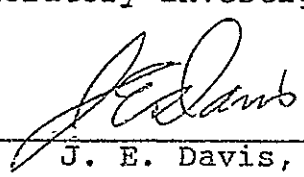

J. E. Davis, Manager
Earth Observations Exploratory
Studies Department

PREPARED BY

Lockheed Electronics Company, Inc.

For

Earth Observations Division
NATIONAL AERONAUTICS AND SPACE ADMINISTRATION
LYNDON B. JOHNSON SPACE CENTER
HOUSTON, TEXAS

October 1977

ABSTRACT

This document is primarily concerned with the performance of the 13.3 GHz airborne scatterometer system which is used as one of several Johnson Space Center (JSC) microwave remote sensors to detect moisture content of soil. The system is analyzed with respect to its antenna pattern; the signal flow in the receiver data channels, and the errors in the signal outputs. The operational principle and the sensitivity of the system, as well as data handling are also described. No discussion is made about the interaction of the transmitted radio frequency (RF) waves with the terrain surface. The dielectric property of the terrain surface, as far as the scatterometer is concerned, is contained in the assumed forms of the functional dependence of the backscattering coefficient σ^o of the incident angle θ.

The consequence of a minor difference in the methods of antenna pattern measurements between 1.6 GHz and 13.3 GHz scatterometer systems was pointed out in the document. It is also found that, because of the rapid antenna gain changes with incident angles in the 13.3 GHz system, the corrections to the variations of the aircraft parameters are crucial in data reduction. Fianlly, a few recommendations are made to improve the overall performance of the scatterometer system.

ACKNOWLEDGEMENT

Special thanks are due to S. C. Reid, who provided all of the laboratory calibration data and many helpful discussions.

CONTENTS

TABLES

FIGURES

LIST OF ACRONYMS AND ABBREVIATIONS

Acronym	
AC	Alternating Current
C	Centigrade
CAD	Computation and Analysis Division
cm	Centimeter
CW	Continuous Wave
dB	deciBel
dBm	deciBels referred to 1 milliwatt
DC	Direct Current
DDC	Data Distribution Center
EOD	Earth Observations Division
ESD	Engineering Systems Division
FM	Frequency Modulation
g	Gram
GDSD	Ground Data System Division
GHz	GigaHertz
GSFC	Goddard Space Flight Center
Hz	Hertz
IR	Infrared
IRIG-A	Inter-Range Instrumentation Group Format-A
JSC	Johnson Space Center
JSME	Joint Soil Moisture Experiment
^{o}K	Degree Kelvin
KHz	KiloHertz
m	meter

Acronym	
MHz	MegaHertz
NASA	National Aeronautics and Space Administration
PCM	Pulse Coded Modulation
pf	picofarad
REC	Record
RF	Radio Frequency
RMS	Root Mean Square
SSBM	Single Side-Band Modulator
TAMU	Texas A&M University
UK	University of Kansas
VSWR	Voltage Standing Wave Ratio
VV	Vertical-Vertical
XMIT	Transmit

1. INTRODUCTION

The NASA/JSC (Johnson Space Center) 13.3 GHz single-polarized airborne scatterometer system has been extensively studied and used for various applications in the past years (refs. 1, 2, 3, 4, 5, and 6). Krishen (ref. 1) and Bradley (ref. 2) used the data obtained from this system over the ocean to estimate the backscattering coefficient σ^o at various incident angles and discussed the relation between σ^o and the ocean wind speed. Rouse (ref. 3) and Parashar et. al. (ref. 4) have demonstrated the capability of the scatterometer system in the sea ice classification work. Dickey et. al. (ref. 5) showed an increase of ~5-7 dB in the backscattered signals as the scatterometer flew from the dry to irrigated parts of the same agricultural field. The system performance studies of the scatterometer based on data measured prior to 1970 were made by Bradley (ref. 2) and by Krishen et. al. (ref. 7). A more recent analysis of the same system was done by Rosenkranz (ref. 8).

Recently, the 13.3 GHz scatterometer and another two scatterometer systems at the frequencies of 0.4 GHz and 1.6 GHz were installed in a NASA C130 aircraft as the additional microwave sensors for the Joint Soil Moisture Experiment (JSME). The antenna gain pattern for the 13.3 GHz system was re-measured at JSC in early 1976. To make a quick assessment of the data quality for each mission, a real-time data processor has recently been added to the system also. With these new feature and measurements in mind, it is the purpose of this report to re-evaluate the performance of the system. In particular, it will be pointed out that there is

a slight difference in the methods of antenna pattern measurements made at JSC for the 13.3 GHz system and at the Physical Sciences Laboratory (PSL) of the New Mexico State University for the 0.4 GHz and 1.6 GHz systems. As a consequence of this small difference in the measurement approach, the data processing equation for the 13.3 GHz system would be different from that for the other two systems, unless the measured antenna patterns for all three systems were brought into conformity by certain coordinate transformations.

This document is organized into six sections. Section 2 deals with the system characteristics, the antenna and the system functional descriptions, the procedures of data handling, and the expected receiver sensitivity at aircraft altitudes. Section 3 gives the scatterometer system analysis. In this section, the data processing equations to estimate σ^{o} are presented and a typical backscattered signal is traced through the receiver channels. Some coefficients appearing in the data processing equations are identified with the newly measured system parameters in the process. The antenna main beam gain contour, beamwidth variations with incident angles, as well as the side-lobe and cross-polarization gain levels are examined and studied in Section 4. Section 5 gives the numerical results. These include the estimates of σ^{o} by two different data processing equations, the presentation of a sample backscattered signal power spectrum data from a recent functional check flight over Lake Livingston, Texas, and an estimate on the precision of the scatterometer system. Finally, the major conclusions of the report and a few suggestions on the future work are contained in Section 6.

Four appendices are included at the end of the document to provide a detail list of the results from the laboratory measurements on the 13.3 GHz scatterometer system parameters, the mixer mathematical model, the function of the ferrite modulator, and a listing of the computer program for the estimation of σ^{o}.

2. SYSTEM DESCRIPTION

2.1 SYSTEM SPECIFICATIONS

The NASA/JSC 13.3 GHz airborne scatterometer is a continuous-wave Doppler radar system (ref. 9), designed to measure the backscattering coefficient σ^o as a function of the angle of incidence θ for various types of the earth's terrain. The scatterometer antenna pattern is fan-shaped which covers the θ range, along the aircraft flight path, of approximately $\pm 5^o$ to $\pm 60^o$ from the nadir direction. The scatterometer receives the backscattered signal at all angles of incidence simultaneously. As a result of the aircraft's forward motion, different Doppler frequency shifts are introduced in the return signals from different θ. The power of the return signals from a ground resolution cell associated with a given θ is finally retrieved by bandpass filtering at the corresponding Doppler frequency during data processing.

The overall system specification and capabilities are given in Table 2-1. The specification of the real-time data processor is not included, because the unit is still under modification and testing. The scatterometer is operated only in the vertical-transmit and vertical-receive mode.

In the next few subsections, the antennae, the operational principle, and the receiver sensitivity are further elaborated. The tape recording system as well as the data handling technique are also briefly described.

TABLE 2-1

THE 13.3 GHz SCATTEROMETER SYSTEM CHARACTERISTICS

Type of System	CW Doppler
Transmit Frequency	13.3 GHz ± 100 MHz
Transmitter Power Output	1.0 Watt
Number of Antennae	Two, one transmit and one receive
Antenna Gain (two-way)	~38 dB
Antenna Beamwidth (two-way)	$\sim 3^{c}$
Antenna Along-Track Coverage	$\sim 120^{o}$ fan beam
Transmitter/Receiver Isolation	~52 dB
Antenna VSWR (Max.)	1.5 = 1
One-Way Side Lobe Level	<20 dB below main beam
Maximum Skew Angle (Antenna Pattern)	$\sim \pm 0.5^{o}$
Polarization	VV
Dynamic Range	~65 dB
Receiver Sensitivity	~150 dBm/Hz
Receiver Noise Figure	20 dB @ 10 KHz
Signal to Noise Figure (1500 ft. altitude)	>10 dB

2.2 THE ANTENNAE

There are two identical antennae in the 13.3 GHz scatterometer system, one of them associated with the transmitter and the other with the receiver. Each antenna is made of a piece of slotted rectangular waveguide. Both antennae were installed underneath the aircraft body between the two wings, with the axes of the waveguides perpendicular to the aircraft roll axis so that the antenna beams were shaped in the cross-track direction. The nominal one-way, cross-track beamwidth is about 3 to 4 degrees as measured from each of the two antenna radiation patterns. The along-track antenna beam coverage is normally from -60° in the aft to $+60^{\circ}$ in the fore direction. There is no apparent aircraft structure present in the region from nadir out to the horizon in both fore and aft directions. Thus, the data collected within both fore and aft antenna beam coverages should be of useable quality.

Some difference in the methods of antenna gain measurements was noted for the 13.3 GHz and 1.6 GHz scatterometers. The coordinate systems used in these measurements were shown in Figure 2-1. The antenna gain measurements for the 1.6 GHz system were made with a conical cut around the axis parallel to the flight direction (i.e., the angle $90^{\circ} - \theta$ remains constant for a given cut). The same measurements for the 13.3 GHz, on the other hand, were made with a conical cut around the axis perpendicular to the flight direction i.e., the angle $90^{\circ} - \phi$ remains constant for a given cut). Because of this difference, the data processing equations for the two

scatterometer systems would be slightly different, as pointed out in Section 3. The antenna gain patterns for the 13.3 GHz system were measured with a mockup to simulate the aircraft frame.

Throughout this report the incident angle θ is always measured from the nadir, positive in the fore direction and negative in the aft direction. The cross track angle ϕ is measured at the location of the antennae from the axis of the aircraft flight as shown in Figure 2-1 for the 13.3 GHz system.

2.3 PRINCIPLE OF OPERATION

The operational principle of the 13.3 GHz scatterometer had previously been described in several reports (refs. 2, 7, and 9). For the sake of signal analysis in the later sections and the completeness of this document, it will be briefly described again in this subsection. Figure 2-2 shows the block diagram of the scatterometer system. It is copied from the report of Reid (ref. 9).

The scatterometer system continuously transmits and receives RF energy at 13.3 GHz through the transmit and receive antennae which respond strongly to the vertically-polarized waves only. The responses to the cross-polarized waves for both antennae are finite but negligibly small (see Section 4). Therefore, unless otherwise specified, the discussion throughout this document refers to the VV (vertically-polarized wave transmission and reception) polarization state only.

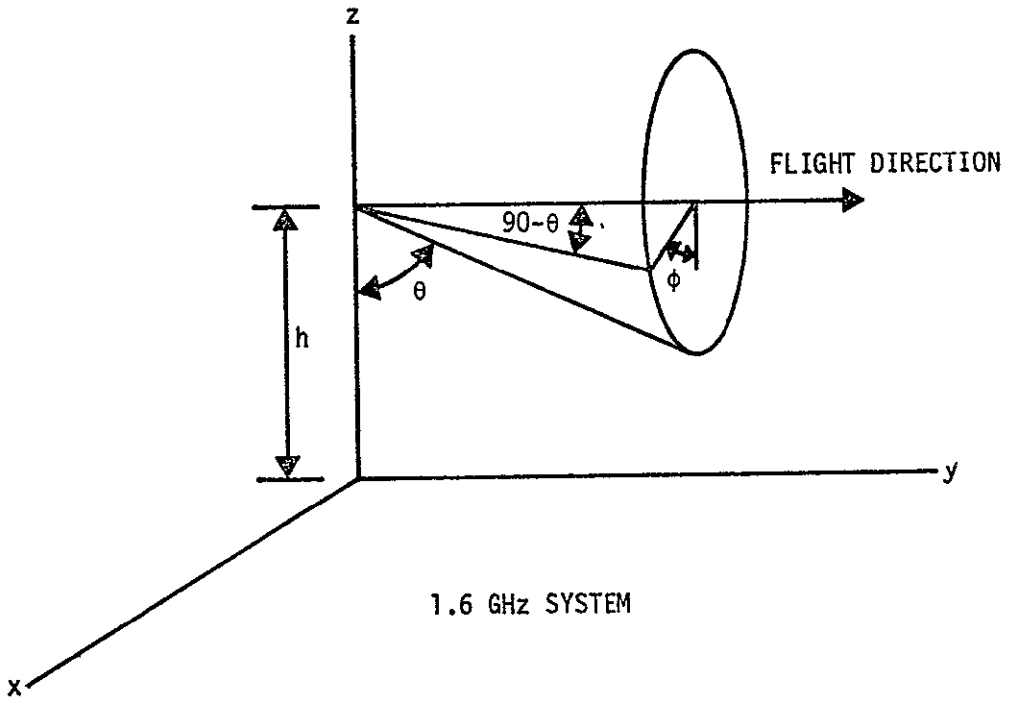

1.6 GHz SYSTEM

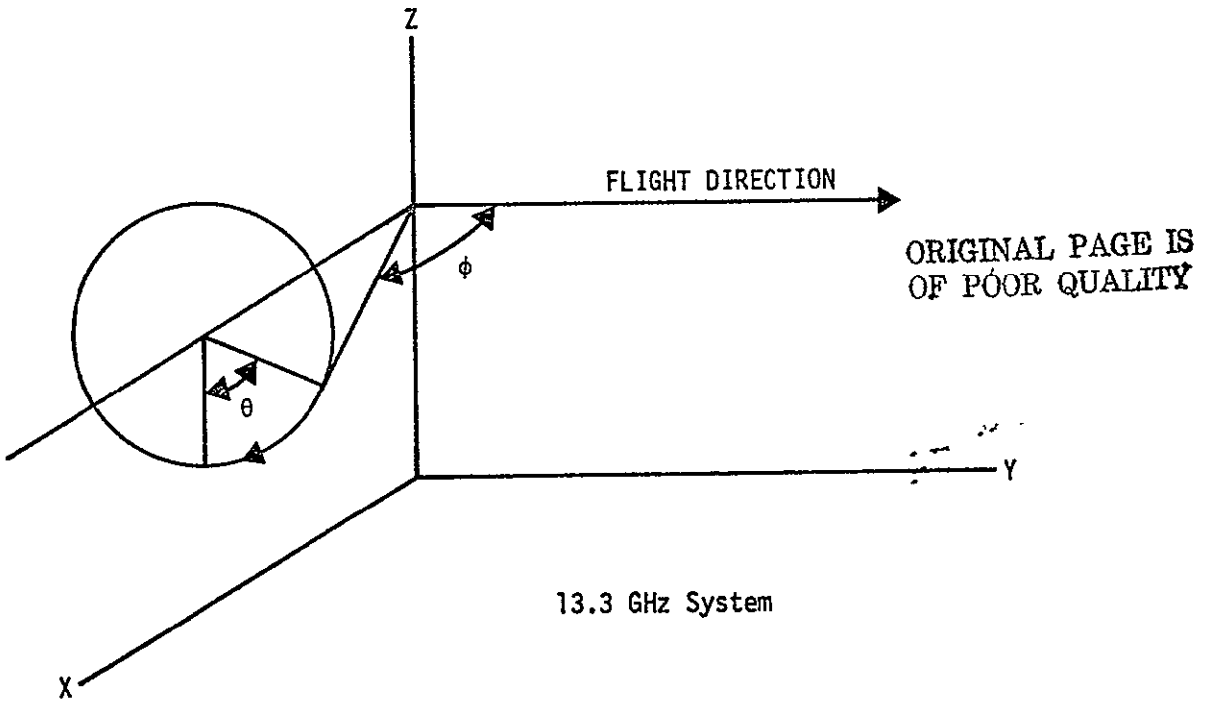

13.3 GHz System

Figure 2-1. – The coordinate systems used in the 1.6-GHz and 13.3 GHz scatterometer antenna pattern measurements.

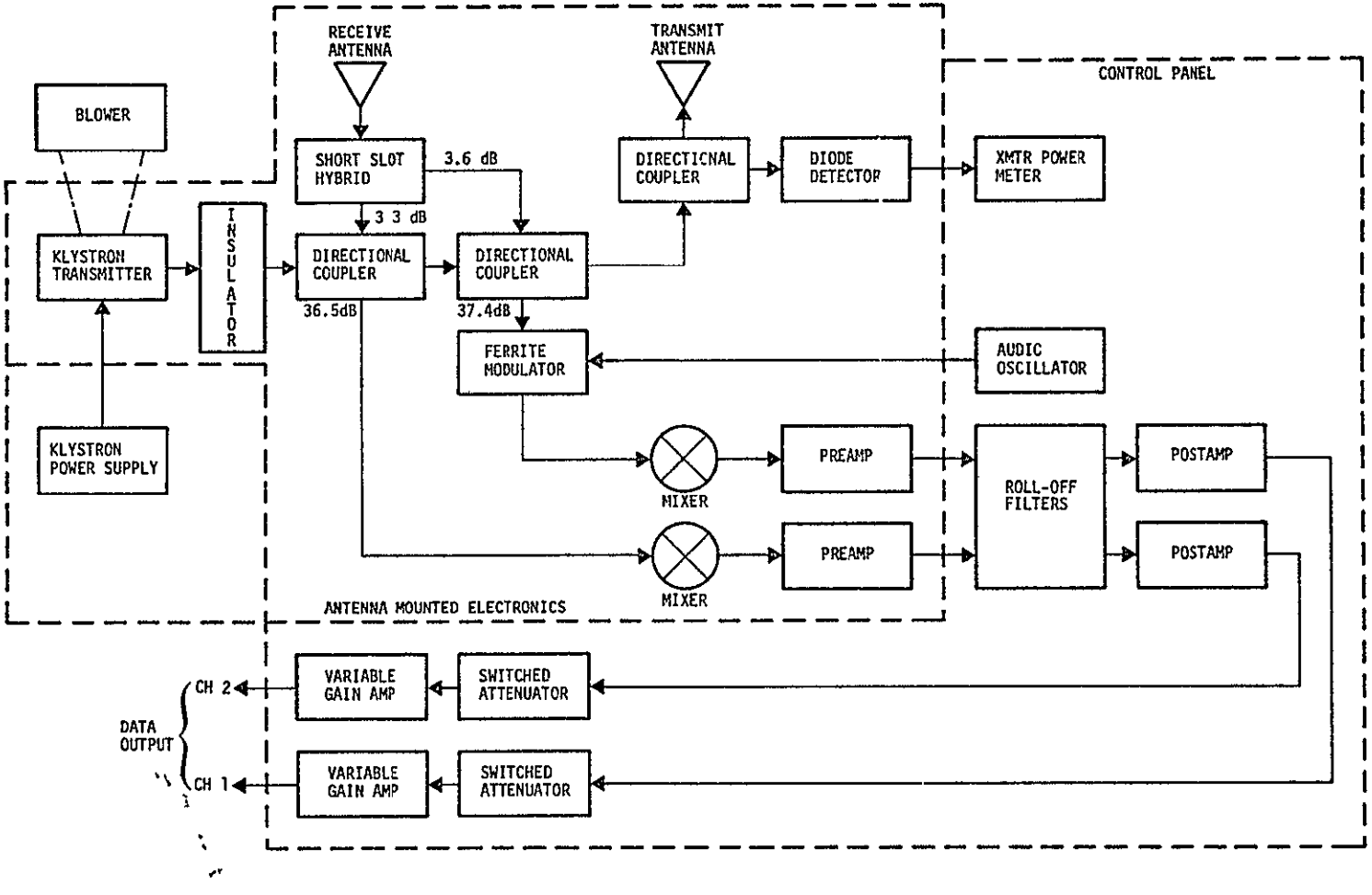

Figure 2-2.— 13.3 GHz scatterometer block diagram.

The backscattered signals are received at all angles of incidence (fore and aft) simultaneously. The received signal is then split into two components by a hybrid coupler, one without phase shift (channel 1) and one with a 90^{o} phase shift (channel 2). A transmitter sample signal (local oscillator signal) is also fed to each of the two data channels through a directional coupler. The combined signals in channel 1 are amplitude modulated after passing through a ferrite modulator driven by an audio oscillator. The modulated signals are mixed in the mixer and the resultant output from this mixing is a zero IF frequency spectrum data which is amplified by a series of audioamplifiers and then recorded on a tape recorder. Except the amplitude modulation by a ferrite modulator, the signal in channel 2 follows the same steps. The resultant output signal is again a zero IF frequency spectrum data which is amplified by a series of audioamplifiers and recorder by the same recorder. The signals from the two data channels are recorded with the same head on the adjacent channels of the magnetic tape to minimize the timing inaccuracy and skew effect. In either one of the two data channels, the fore and aft signals are folded in the mixer. As a result, the output signals from the two data channels are in phase quadrature with each other. During data reduction, these phase quadrature data are digitized and Fast Fourier transformed. Then the summation and difference of the transformed signal spectra from the two data channels are taken to recover the fore and aft Doppler signals.

As indicated in Figure 2-2, the power level of the transmitter sample signal in Channels 1 and 2 were measured to be 37.4 dB and 36.5 dB, respectively, below the power level of the transmitter. The backscattered signal in the receiver was also not split evenly

into the two data channels, being 3.6 dB and 3.3 dB in Channels 1 and 2 respectively below the backscattered signal. The slight unevenness of both backscattered and transmitter sample signals would not affect the quality of the data, because the final gain adjustment could be made just before the data was recorded on the tape recorder.

With the addition of the real-time data processor, the data quality of a given flight mission could be assessed quickly. Including this addition, the block diagram of the entire 13.3 GHz scatterometer system is shown in Figure 2-3. A junction box is provided to handle all the data flow. The backscattered signals in Channels 1 and 2 and the ADAS data, after passing through the junction box, are recorded on the tape recorder No. 1. This tape recorder also records data from both 0.4 GHz and 1.6 GHz scatterometers as discussed in the next subsection. The backscattered signals and ADAS data are also channeled to the real-time data processor for immediate processing. The results from this processing are sent back to the junction box and plotted on a strip chart recorder. The 4-channel range expander provides adequate dynamic range to handle the processed data. The ADAS and the processed data are also recorded by the tape recorder No. 2.

To aid in the association of the backscattered signal at a given time to a ground location, a Zeiss camera system was installed in the aircraft to take the IR pictures of the terrain at approximately 4 sec intervals. The time of the data and picture taking enters

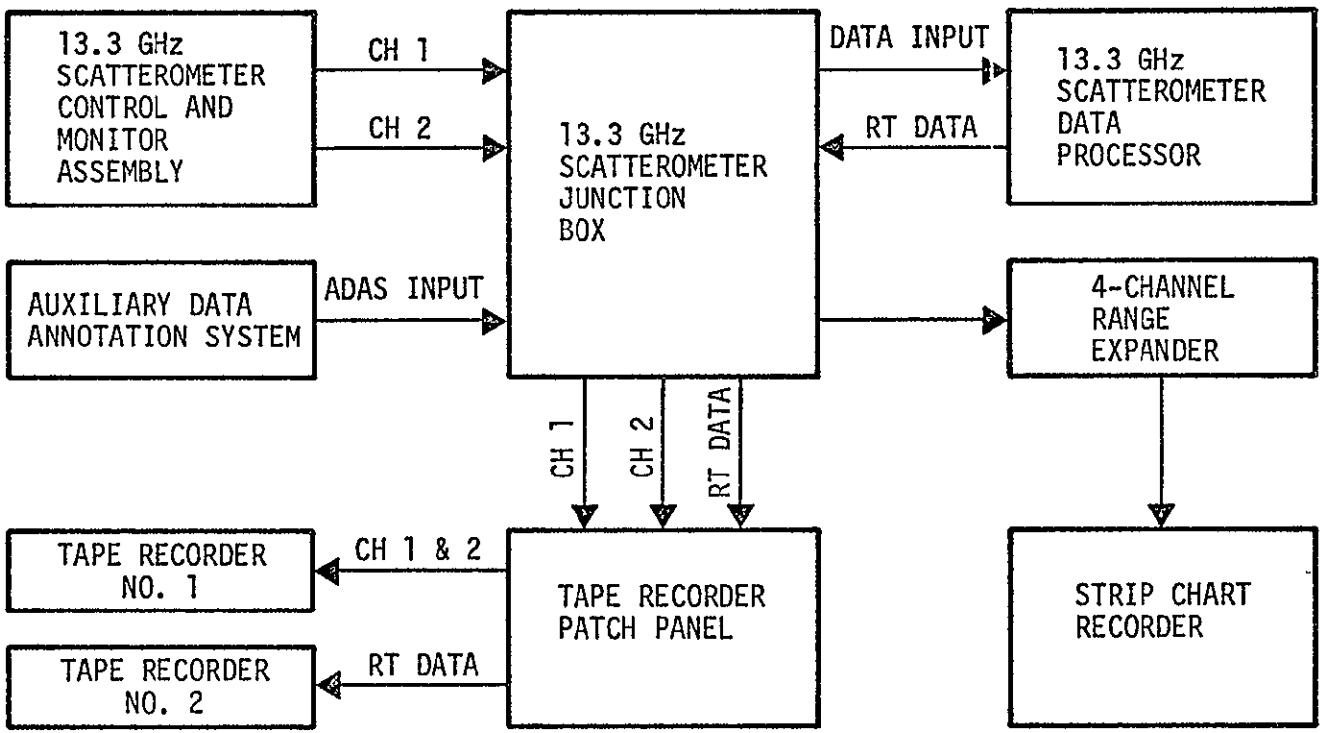

Figure 2-3.— The block diagram of the 13.3 GHz scatterometer real-time data processing.

in both the tape recording system and the picture frames. By comparing the times recorded in both the magnetic tape and the IR pictures, the backscattered signal at a given Doppler frequency (or incident angle) can be identified with a ground location, subject to a reasonable uncertainty.

2.4 THE TAPE RECORDING SYSTEM

The output of the scatterometer is recorded by a Mincom Series 110 Recorder/Reproducer System, Wideband Group I. The system is a solid state, compact, portable unit which has a bi-directional tape transport and directly interchangeable signal electronics plug-in modules for FM recording. It records data on a 1-inch magnetic tape with 14 data channels and with a carrier modulating frequency of 108 KHz. It has a bandwidth coverage from DC to 20 KHz. The signal to noise ratio is ~40 dB and the speed of the data recording is 30 inches per second. The specification of the system is given in Table 2-2.

The input level of the tape recorder is set at 1 volt RMS nominal, but is adjustable to produce full scale modulation between 0.5 and 10 volts peak to peak. The output level is 1 volt RMS nominal into a 50-ohm load. It is also adjustable from 0 to 1.5 volts RMS. The input impedance is 10,000 ohms nominal shunted by 330 pico-farads maximum unbalanced to ground.

The tape recorder No. 1 (see Figure 2-3) is shared by three air-borne scatterometers at the frequencies of 0.4 GHz, 1.6 GHz, and

TABLE 2-2. - SPECIFICATIONS OF THE TAPE RECORDER/REPRODUCER SYSTEM USED FOR JSME (WIDEBAND GROUP I)

Magnetic Tape Size	1" in width and 14" in diameter, containing 9,200' of tape
Tape Speed	30 ips (inches per second)
Tape Speed Accuracy	0.03 ips
Time Base Error	0.6 sec at 50 KHz reference frequency
Start and Stop Time	5 sec.
% Flutter (Maximum Cumulative) at 30 ips	0.30 peak to peak at flutter bandwidth of 0.2 to 5 KHz
Center Carrier Frequency	108 KHz
Frequency Response	DC to 20 KHz
Signal to Noise Ratio	40 dB (RMS/RMS)
Input Level	1 volt RMS nominal. Adjustable for input levels between .5 & 10 volts peak-to-peak
Output Level	1 volt RMS into a 50 ohm load. Adjustable from 0 to 1.5 volts RMS
Input Impedance	10,000 ohms nominal shunted by 330 pf maximum unbalanced to ground
Output Impedance	50 ohms maximum, unbalanced to ground
Ambient Temperature Range	0° to 50°C at sea level
Thermal Drift	After 15 min. warmup, less than $\pm 0.1\%/C^{\circ}$ in full scale output voltage change, over a temperature range of 0° to 50°C
DC Linearity	Within ±0.5% of peak-to-peak deviation from the best zero based straight line
Total Harmonic Distortion	< 1% at 1 KHz
Humidity	Up to 95% relative humidity without condensation

13.3 GHz. The assignments of the channel number for various data outputs of the scatterometers are shown in Figure 2-4. The 13.3 GHz scatterometer outputs are recorded on two adjacent data channels (11 and 13) of the same head.

The time of data taking is recorded through IRIG Standard Time Code and Aircraft Data Acquisition System (ADAS) in channels 9 and 2 respectively. In addition to the time information, ADAS also acquires the aircraft parameters such as altitude, speed, and roll, pitch and drift angles.

The time and aircraft parameters provided by ADAS are recorded sequentially in PCM format and frequency modulated at 225 KHz. All of this information is derived during data reduction and, one way or another, is used in the data processing for the derivation of backscattering coefficient σ^o.

2.5 RECEIVER SENSITIVITY

One way to estimate the sensitivity of the scatterometer system is by examining the signal to noise ratio at the receiver output. The signal at the receiver output can be evaluated by using the data processing equation described in Section 4 and the measured system loss factor. For the convenience of a numerical estimate, Eq. (3-3) is repeated and simplified here:

$$P_r = \frac{P_t \lambda^2}{(4\pi)^3} \int_A \frac{G_t \sigma^o G_r}{R^4} \, dA = \frac{P_t \lambda^2 \bar{G}_t \bar{\sigma}^o \bar{G}_r}{(4\pi)^3 \bar{R}^4} A \qquad (2\text{-}1)$$

Figure 2-4.— Channel assignment of signal outputs for three scatterometers.

where a bar over a given symbol indicates the average value of that parameter over a ground resolution cell A. The numerical values of all the parameters in the above equation were evaluated and entered in Table 2-3 for the estimate of the receiver output signal level. The aircraft altitude and speed were assumed to be ~460m and ~80 m/sec, respectively. The incident angle was taken to be 60^{o} where low signal return was expected. The along-track ground cell length used in the area calculation was ~25m which, at 60^{o} incident angle and 80 m/sec aircraft speed, corresponded to a bandwidth of ~48 Hz. The cross-track two-way beamwidth as obtained from Figure 4 - 4 was ~3.9^{o}. The power loss from the transmitter to the transmit antenna was measured to be ~0.5 dB (S. C. Reid, personal communication). The σ^{o} value at 60^{o} incident angle was derived from Figure 3-4; the smooth water valve was used for low signal return. All of the remaining parameters appeared in Eq. (2-1) are self-explanatory.

The sum (is dB) of the radiated power and the propagation constant gives the received power at the antenna terminal. Since there is no receive antenna feed line loss, the receiver signal output is -120.9 dBm. The amplification factor and the rolloff function were not entered in this calculation because both of them applied to the signal and noise equally and cancelled out when signal to noise ratio was taken.

For the calculation of the receiver noise level, the ambient temperature was assumed to be ~290^{o} K. The Boltzman's constant

TABLE 2-3. - THE 13.3 GHz SCATTEROMETER SIGNAL TO NOISE RATIO

Output of the Transmitter	+30 dBm
Transmit Antenna Feed Line Loss	-0.5 dB
RADIATED POWER	+29.5 dBm
λ^2 (Wavelength 0.02255 m)	-32.9 dB
$G_t G_r$ (Gain at $\theta = 60^\circ$)	+27.0 dB
σ° (at $\theta = 60^\circ$)	-24.8 dB
$(1/4\ TV)^3$	-33.0 dB
$(1/R)^4$ (Range)	-118.6 dB
A (Area Element)	31.9 dB
PROPAGATION CONSTANT	-150.4 dB
RECEIVER SIGNAL OUTPUT	-120.9 dBm
kT	-174.0 dBm
Bandwidth Corresponding to Resolution Cell A	16.8 dB
Receiver Noise Figure	18.0 dB
RECEIVER NOISE POWER	-139.2 dBm
SIGNAL TO NOISE RATIO	18.3 dB

k is 1.38×10^{-23} joule/^{o}K. The noise figure of 18 dB was obtained from the laboratory measurements at 6 KHz (see Appendix A). Summing all of these factors, the receiver noise output over the 48 Hz bandwidth is estimated to be -139.2 dBm, which results in a signal to noise ratio of ~18.3 dB.

For operation over land or for small angle of incidence, the signal to noise ratio is expected to improve. For example, σ^{o} over land at 60^{o} incident angle could be ~5.4 dB (see Figure 3-4) instead of -24.8 dB for water. The signal to noise ratio in that case would be ~37.7 dB rather than ~18.3 dB. The signal to noise ratio at smaller incidence angles could be better than 40 dB. However, the signal to noise ratio of the tape recorder system described in the previous subsection is ~40 dB, which represents the best value attainable with the 13.3 GHz scatterometer and the data recording system.

2.6 THE SCATTEROMETER DATA HANDLING

A fair amount of data handling is required before the processed scatterometer data can be delivered to the principal investigators for studies and interpretations. Figure 2-5 gives a flow chart of the scatterometer data handling. The analog tape, which contains the data for all three scatterometer systems (at frequencies of 0.4 GHz, 1.6 GHz, and 13.3 GHz) from a given mission, is duplicated at Ground Data System Division (GDSD). The aircraft parameters such as roll, drift, pitch, altitude, and speed are also extracted and prepared in a tabular form at GDSD. The copies

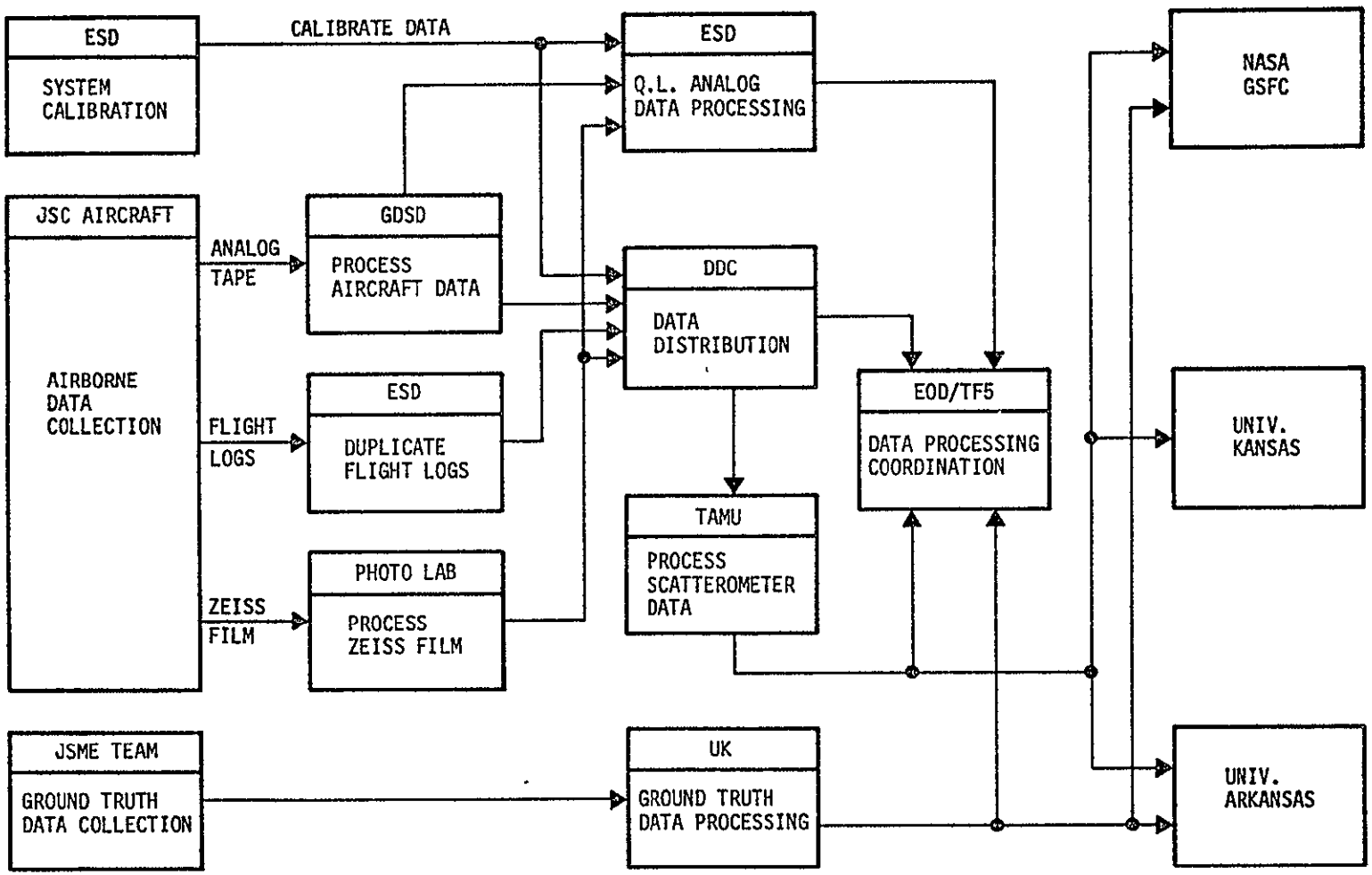

Figure 2-5.— Scatterometer data handling flow chart.

of the analog tape and the tables of aircraft parameters are delivered to the Engineering Systems Division (ESD) and the Data Distribution Center (DDC), respectively for a quick-look processing and for distribution. The results from the quick-look analog processing are examined for data quality of the mission at the SF5 branch of the Earth Observations Division (EOD/SF5).

In addition to the recording of the scatterometer data and the aircraft parameters, the flight logs and the Zeiss IR film are also generated in a mission. The flight logs contain information on the occurrence of events for the entire mission, while the IR film shows the ground scene of all the aircraft flight lines of interest. The IR film is processed and copies made at the JSC Photo Laboratory, and the flight logs are duplicated at ESD. Copies of both the IR film and the flight logs are delivered to DDC for further distribution. ESD also receives a copy of the IR film to aid in the quick-look data processing.

Generally, a system calibration is performed on the scatterometers in ESD before a major mission takes place. The calibrate constants are needed in both quick-look and final data processings at ESD and Texas A & M University (TAMU), respectively. TAMU receives a copy each of the analog tape, the aircraft parameters, the flight logs, and the calibrate constants to do the data processing with a digital method. The final outputs from the TAMU processor are plots and/or listings of the time history of the backscattering coefficient σ^{o}. These outputs are distributed to the principal

investigators at NASA/GSFC, University of Kansas, and the University of Arkansas for further studies. EOD/SF5 also receives a copy for bookkeeping and evaluation purposes.

The ground truth data collection is performed jointly by all the parties involved in the JSME mission. The collected data are processed and organized at the University of Kansas. The final ground truth data outputs are tabulated and distributed to all the principal investigators involved and to EOD/SF5 at JSC.

Finally, the flow and distribution of the 13.3 GHz scatterometer data processed by the real-time processor have not been determined by the time of this writing. The handling of those data may be decided in the near future.

3. SYSTEM ANALYSIS

3.1 DATA PROCESSING EQUATIONS

The power P_r reflected from a target and collected by a receiving antenna can be expressed in terms of the radar parameters as (see, e.g., Ref. 12):

$$P_r = \frac{P_t G_t G_r \sigma \lambda^2}{(4\pi)^3 R^4} \qquad (3\text{-}1)$$

where

P_t = power transmitted by the radar

G_t = gain of the transmitting antenna in the direction of the target

G_r = gain of the receiving antenna in the direction of the target

σ = radar cross-section of the target

λ = radar wavelength

R = distance between the radar and the target

For remote sensing of a surface terrain by an airborne radar system such as the NASA 13.3 GHz scatterometer, it is more appropriate to use the backscattering coefficient σ^o (differential cross section per unit area) rather than σ. σ^o and σ are related through the differential area element dA by

$$d\sigma = \sigma^o \, dA \qquad (3\text{-}2)$$

In terms of this definition Eq. (3-1) becomes

$$P_r = \int_A \frac{P_t G_t G_r \sigma^o \lambda^2}{(4\pi)^3 R^4} dA \qquad (3\text{-}3)$$

The power $P_r(\theta)$ observed at a given central Doppler frequency $f_D(\theta)$ and within a bandwidth $\Delta f_a(\theta)$ is uniquely related to a ground cell A, as shown in Figure 3-1, through the relation

$$f_d(\theta) = \frac{2V}{\lambda} \sin \theta \qquad (3\text{-}4)$$

and

$$\Delta f_d(\theta) = \frac{2V}{\lambda} \cos\theta \Delta\theta \qquad (3\text{-}5)$$

where V is the speed of the aircraft. The two isodopplers indicated in Figure 3-1 are defined by the two Doppler frequencies at $f_d + \Delta f_d$ and $f_d - \Delta f_d$. For numerical computations described in section 5, the ground cell $A(\theta)$ is divided into N elements and Eq. (3-3) can be rewritten as

$$P_r(\theta) = \frac{P_t \lambda^2}{(4\pi)^3} \sum_{i=1}^{N} \frac{G_{ti}(\theta)\, G_{ri}(\theta)\, \sigma_i^{\circ}(\theta)}{R_i^4(\theta)} \Delta A_i \qquad (3\text{-}6)$$

The power density $W_r(\theta)$ is simply

$$W_r(\theta) = \frac{P_r(\theta)}{\Delta f_d(\theta)} = \frac{P_t \lambda^2}{\Delta f_d(\theta)\ (4\pi)^3} \sum_{i=1}^{N} \frac{G_{ti}(\theta)\, G_{ri}(\theta)\, \sigma_i^{\circ}(\theta)}{R_i^4(\theta)} \Delta A_i \qquad (3\text{-}7)$$

Two factors have been omitted in the above discussion. They should be considered before the final receiver output is obtained and interpreted. First, the attenuation of the RF power due to the two-way path of propagation is not included. The magnitude of this attenuation, in absence of heavy precipitation, depends on the amounts of oxygen and water vapor along the propagation path. At Skylab altitudes ($\sim$235 nautical miles) and assuming a

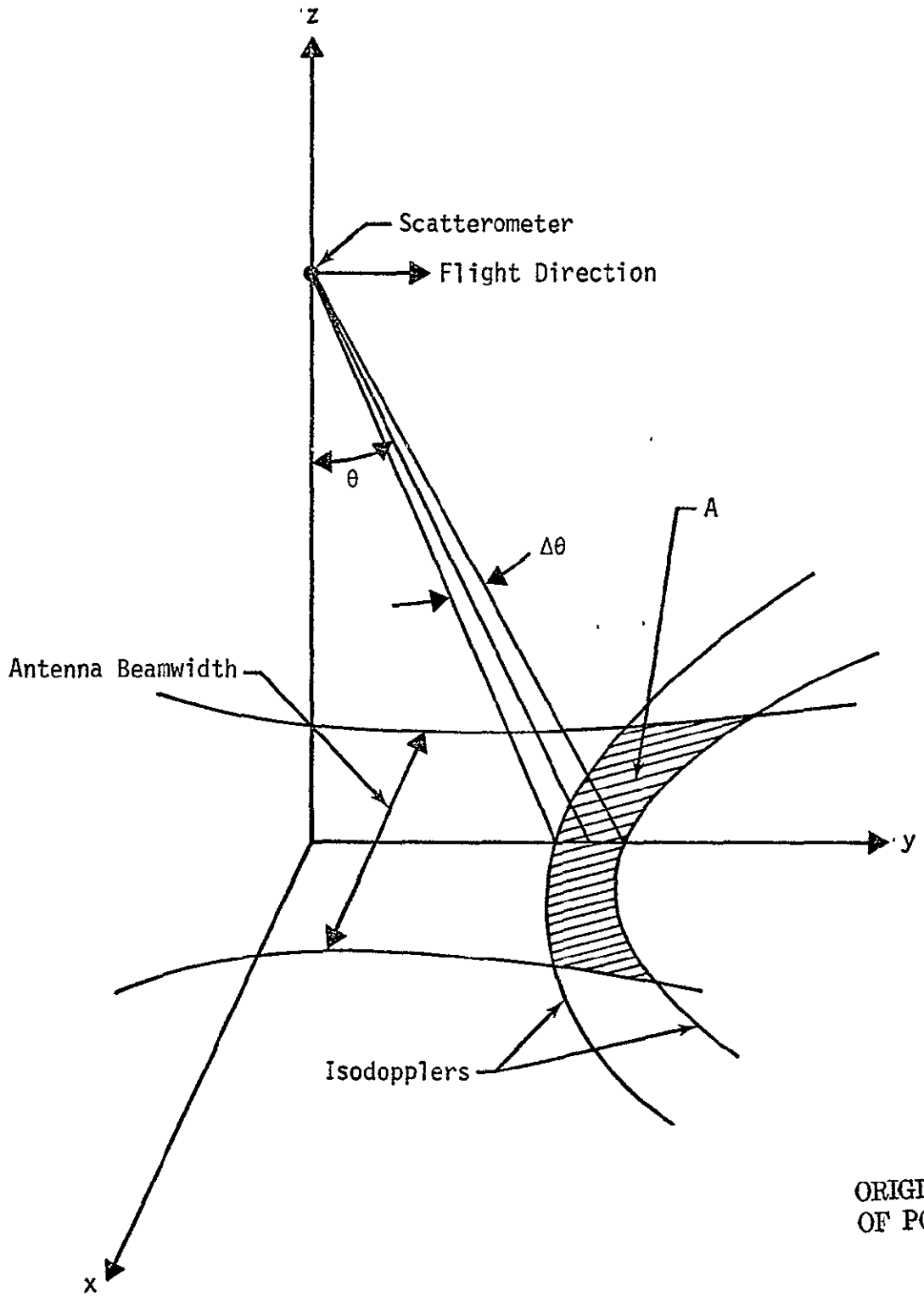

Figure 3-1.— The resolution cell as defined by Doppler frequency bandwidth and antenna beamwidth.

water vapor density of $\sim$ 7.5 gm/m^3, the two-way attenuation of the S-193 radar at 13.9 GHz and at $\sim$48° incident angle was estimated to be only 0.24 dB (ref. 13). For most of the mission carried out by the C130 aircraft so far, the cruising altitude was $\sim$ 1,500 feet. Therefore, the loss due to atmospheric attenuation can be completely neglected. Secondly, P_r as given in Eq. (3-6) is the power of the back-scattered signal at the receiver input. As the signal passes through the receiver data channels, it experiences losses as well as gains due to the presence of many subsystems. These gains and losses are automatically taken care of by the presence of a calibrate signal at 12 KHz as explained in the next few subsections.

To derive the backscattering coefficient σ^o as a function of incident angle θ from Eq. (3-7) requires an iteration process. First, a functional dependence of σ^o on θ has to be assumed. Then the power density $W_r(\theta)$ of the backscattered signal is calculated from Eq. (3-7) for a series of θ and $\Delta\theta$. The calculated $W_r(\theta)$ is compared with the power spectrum derived from observations. If the power spectra from computation and from observation do not match well over the incident angles of interest, another form of $\sigma^o(\theta)$ is assumed and the procedure repeated. The final functional dependence of σ^o on θ is ascertained when best match between the computational and the observational power spectra is obtained.

A simple, direct, and most used approach of determining σ^o as a function of θ is to first associate a ground resolution cell

$A(\theta)$ with a single average value of $\sigma^o(\theta)$, as shown in Figure 3-2, and then express $\sigma^o(\theta)$ in terms of all measurable parameters. From this figure,

$$d_1 = R\Delta\phi$$

and

$$d_2 = \frac{R\Delta\theta}{\cos\theta} \tag{3-8}$$

$$A(\theta) = d_1 d_2 = \frac{R^2\Delta\phi\Delta\theta}{\cos\theta}$$

Substituting the expression for $\Delta\theta$ in Eq. (3-5) into Eq. (3-8), the area of the ground cell becomes

$$A(\theta) = \frac{R^2\lambda\Delta\phi\Delta fd}{2V\cos^2\theta} \tag{3-9}$$

and the backscattered power from this area is

$$P_r(\theta) = \frac{P_t G_t(\theta) G_r(\theta) \sigma^o(\theta) \lambda^3 \Delta\phi\Delta fd}{(4\pi)^3 2Vh^2} \tag{3-10}$$

Expressed in terms of $\sigma^o(\theta)$, Eq. (3-10) becomes

$$\sigma^o(\theta) = \frac{(4\pi)^3 2Vh^2 W_r(\theta)}{P_t G_t(\theta) G_r(\theta) \lambda^3 \Delta\phi} \tag{3-11}$$

where the aircraft altitude $h = R\cos\theta$ and Eq. (3-7) was used.

Both approaches for the determination of σ^o versus θ relationship are attempted in section 5 where the numerical calculation is performed. A comparison is made on the results from both approaches.

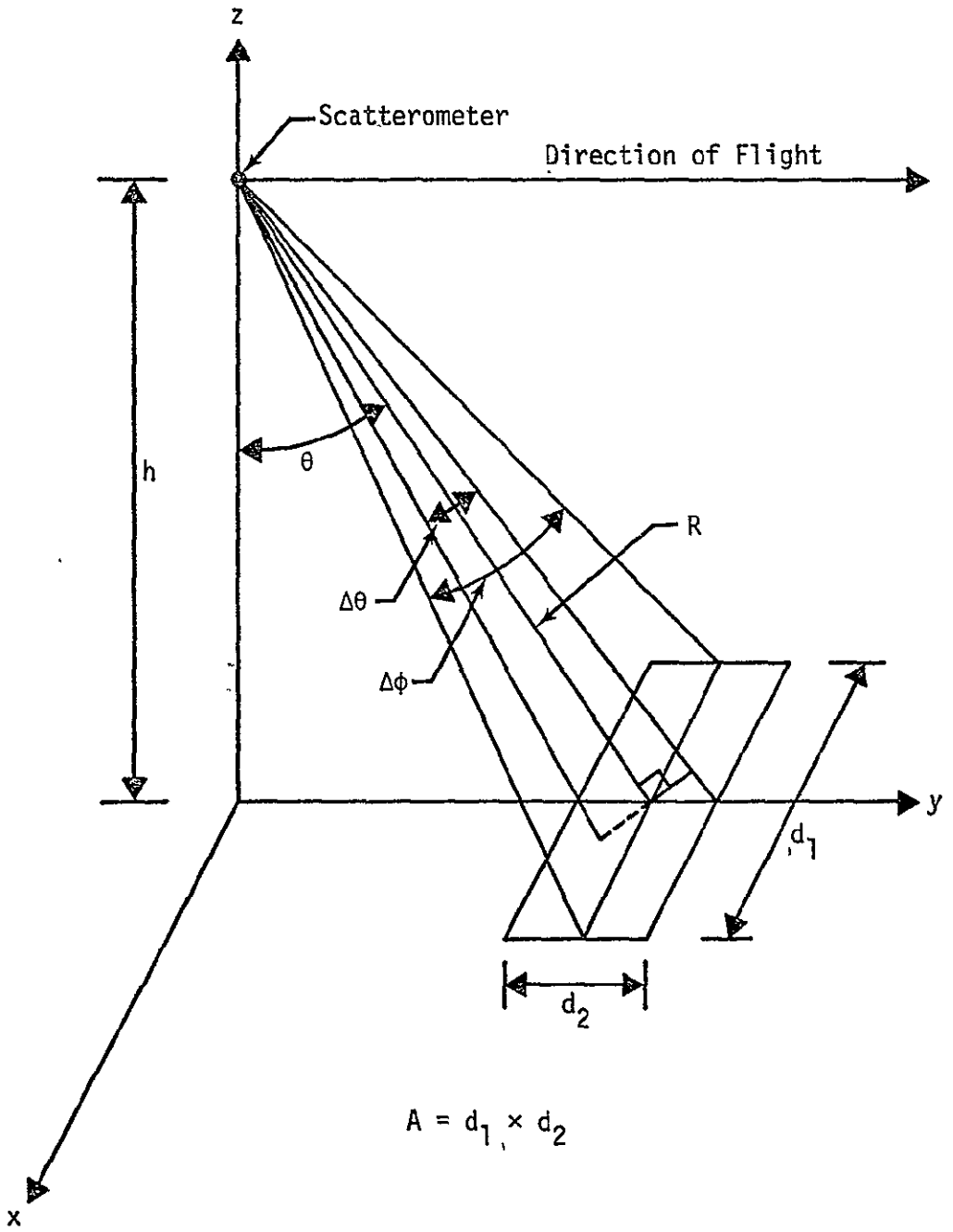

Figure 3-2.— Geometry of a scatterometer ground resolution cell.

The backscattered signal in the receiver data channels is further analyzed and the backscattering coefficient σ^o are discussed in the following subsections. The antenna gain pattern, side lobe level and coupling effect are discussed in detail in section 4.

3.2 RECEIVER SIGNAL ANALYSIS

To develop a comprehensive mathematical model for the signal response of the scatterometer system requires a complete knowledge on the characteristics of each of the many subsystems shown in the block diagram of Figure 2-3. These characteristics include the gains, bandwidths, and noise figures of all amplifiers, the gains and bandwidths of all filters, to name just a few. To make new measurements on all of these parameters may be costly and time consuming, while to develop a mathematical model based on old values of these parameters may not be appropriate, especially when some of the components were replaced over the past years. Consequently, a different approach is attempted here to derive a practical transfer function of the whole system, with the aid of some new measurements on a few key system parameters.

The approach follows closely with those attempted for the 13.3 GHz airborne scatterometer system by Krishen et al., (ref. 7) and by Bradley (ref. 2 and for the 1.6 GHz system by Wang (ref. 11). The backscattered signal is followed through all major subsystems. The final outputs from the receivers contain factors such as the gains of the amplifiers, the coefficients of the ferrite modulators, and the gains of mixers and filters, which are combined and

identified with the key system parameters recently measured in the laboratory (see Appendix A).

Assuming that the continuous wave at frequency ω_o at the vertical transmitter port is represented by

$$V_t = V_o \cos \omega_o t \tag{3-12}$$

The voltage at the input of the vertical receiver is

$$V_r = C_f \cos \left((\omega_o + \omega_d)t + x_f \right) + C_a \cos \left((\omega_o - \omega_d)t + x_a \right) \tag{3-13}$$

where

C_f = amplitude of the received signal in fore direction, in volts

C_a = amplitude of the received signal in aft direction, in volts

ω_d = the Doppler shift corresponding to fore and aft beam at a particular angle of incidence, in radians/sec

x_f = the phase shift introduced by the path length and the rough surface in the fore beam, in radians

x_a = the phase shift introduced by the path length and the rough surface in the aft beam, in radians

The direct leakage of the signal from transmitter to receiver at frequency ω_o is not included in Eq. (3-13) for reason given in section 4.

The hybrid coupler in the receiver channel divides the input signal equally into two parts, one without phase shift and the other with a 90^{o} phase shift. The output signal from the hybrid coupler can be written as

$$V_{1c} = \frac{k_1}{\sqrt{2}}\left[C_f \cos\left((\omega_o + \omega_d)t + x_f\right) + C_a \cos\left((\omega_o - \omega_d)t + x_a\right)\right] \tag{3-14a}$$

$$V_{2c} = \frac{k_2}{\sqrt{2}}\left[C_f \sin\left((\omega_o + \omega_d)t + x_f\right) + C_a \sin\left((\omega_o - \omega_d)t + x_a\right)\right] \tag{3-14b}$$

where V_{1c} and V_{2c} are the output signal voltages for the channel (channel 1) without phase shift and the channel (channel 2) with 90^{0} phase shift, respectively. k_1 and k_2 take care of the loss in the possible unbalance in the signal power division of the hybrid coupler. There exists an asymmetry between channels 1 and 2 as shown in Figure 2-2. In channel 2, the backscattered signal from the hybrid output is directly mixed with the transmitter sample signal in a mixer. In channel 1, however, the transmitter sample signal and the backscattered signal are modulated by a 12 KHz calibrate signal through a ferrite modulator. The signal from the ferrite modulator output is then mixed in the channel 1 mixer. The voltage of the transmitter sample signal is

$$V_s = \rho V_o \cos \omega_o t \tag{3-15}$$

and the signal voltage at the mixer inputs can be written as (see Appendix B):

$$V_{1f} = \frac{\alpha k_1}{\sqrt{2}} \left[C_f \cos\left((\omega_o + \omega_d)t + x_f\right) + C_a \cos\left((\omega_o - \omega_d)t + x_a\right) + \frac{\sqrt{2}\,\rho_1 V_o}{k_1} \cos \omega_o t + \frac{\sqrt{2}\,\gamma \rho_1 V_o}{k_1} \cos \omega_c t \cos \omega_o t \right] \quad (3\text{-}16a)$$

$$V_{2f} = \frac{\alpha k_2}{\sqrt{2}} \left[C_f \sin\left((\omega_o + \omega_d)t + x_f\right) + C_a \sin\left((\omega_o - \omega_d)t + x_a\right) + \frac{\sqrt{2}\,\rho_2 V_o}{k_2} \cos \omega_o t \right] \quad (3\text{-}16b)$$

Here ρ_1 and ρ_2 gives the magnitudes of the amplitude attenuation in the transmitter signal for channels 1 and 2 respectively. ω_c is the angular frequency of the calibrate signal. α and $\alpha\gamma$ ($\gamma << 1$) are the DC and AC gains of the ferrite modulator, respectively.

After the mixers, the output signal voltages from both channels are (see Appendix C):

$$V_{1m} = \frac{k_1 \beta_1 \rho_1 V_o}{\sqrt{2}} \left[C_f \cos(\omega_d t + x_f) + C_a \cos(\omega_d t - x_a) + \frac{2\,\gamma \rho_1 V_o}{k_1} \cos \omega_c t \right] \quad (3\text{-}17a)$$

$$V_{2m} = \frac{k_2 \beta_2 \rho_2 V_o}{\sqrt{2}} \left[-C_f \sin(\omega_d t + x_f) + C_a \sin(\omega_d t - x_a) \right] \quad (3\text{-}17b)$$

where β_1 and β_2 take care of the conversion losses of the mixers in channels 1 and 2, respectively. The signal voltages as expressed in Equations (3-17a) and (3-17b) are amplified by the series of audio-amplifiers in their respective receiver channels.

They also suffer attenuation through the presence of the switches and filters. If the total gains (before variable gain amplifiers) are G_1 and G_2, respectively, the variable gain amplifiers are adjusted such that

$$G = \beta_1 k_1 \rho_1 V_o G_1 G_{1v} = \beta_2 k_2 \rho_2 V_o G_2 G_{2v} \tag{3-18}$$

where G_{1v} and G_{2v} are the gains of the variable gain amplifiers in channel 1 and 2, respectively. The signal voltages at the variable gain amplifier output are

$$V_{1v} = \frac{G}{\sqrt{2}} \left[C_f \cos(\omega_d t + x_f) + C_a \cos(\omega_d t - x_a) + \frac{^2 \gamma \rho_1 V_o}{k_1} \cos \omega_c t \right] \tag{3-19a}$$

$$V_{2v} = \frac{G}{\sqrt{2}} \left[-C_f \sin(\omega_d t + x_f) + C_a \sin(\omega_d t - x_a) \right] \tag{3-19b}$$

The signals as expressed by Equations (3-19a) and (3-19b) are recorded by a tape recorder on two adjacent tracks of the same head. If additional gain unbalance is introduced by the tape recorder, it can be adjusted again in the data reduction. Since only the relative power levels of the backscattered and the calibrate signals are used in the calculations of the backscattering coefficients, the gain adjustment does not affect the final results.

The fore and aft Doppler signals are separated in the process of data reduction. The recorded data are first digitized by an analog-to-digital converter. The Fast Fourier Transform (FFT)

is then applied to the digitized data to convert the signals from the time domain to the frequency domain. The frequency spectra of the signals given by Equations (3-19a) and (3-19b) after the application of the FFT are:

$$V_1 = \frac{G}{\sqrt{2}} \left[C_f\{\delta(f - f_d) \cos x_f - j\delta(f - f_d) \sin x_f\} + C_a\{\delta(f - f_d) \cos x_a + j\delta(f - f_d) \sin x_a\} + \frac{\sqrt{2}\gamma\rho_1 V_o}{k_1} (f - f_c) \right] \quad (3\text{-}20a)$$

$$V_2' = \frac{G}{\sqrt{2}} \left[-C_f\{\delta(f - f_d) \sin x_f + j\delta(f - f_d) \cos x_f\} + C_a\{-\delta(f - f_d) \sin x_a + j\delta(f - f_d) \cos x_a\} \right] \quad (3\text{-}20b)$$

where $j = \sqrt{-1}$, $f = \frac{\omega}{2\pi}$, and $\delta(f - f_d)$ is the Dirac delta function. In the above expressions, the double-sided spectra (with both positive and negative frequencies) after the FFT are converted to the single-sided spectra by the application of the power scaling factor of 2 (ref. 13). The signal voltage densities, E_f and E_a, (in volts per Hz) at Doppler frequency f_d in the fore and aft direction are obtained by forming the following expressions.

$$E_f = C_f G = \sqrt{\tfrac{1}{2}\left[\{R_e(V_1) - I_m(V_2)\}^2 + \{R_e(V_2) + I_m(V_1)\}^2\right]} \quad (3\text{-}21a)$$

$$E_a = C_a G = \sqrt{\tfrac{1}{2}\left[\{R_e(V_1) + I_m(V_2)\}^2 + \{R_3(V_2) - I_m(V_1)\}^2\right]} \quad (3\text{-}21b)$$

The calibrate signal E_c (in volts per Hz) is given by

$$E_c = \frac{G\gamma\rho_1 V_o}{k_1} \quad (3\text{-}22)$$

From Equations (3-21b) and (3-22), the received power density (in watts per Hz) is

$$W_{ra}(f_d) = \frac{C_a^2}{2} = \tfrac{1}{2}\left(\frac{\gamma\rho_1 V_o}{k_1}\right)^2 \left(\frac{E_a}{E_c}\right)^2 \qquad (3\text{-}23)$$

Since the transmit power P_t is proportional to V_o^2, Eq. (3-23) can be rewritten as

$$W_{ra}(f_d) = \frac{A}{2}\left(\frac{\gamma\rho_1}{k_1}\right)^2 \left(\frac{E_a}{E_c}\right)^2 P_t = \frac{P_t}{K}\left(\frac{E_a}{E_c}\right)^2 \qquad (3\text{-}24)$$

where K is a measurable quantity in the laboratory, as discussed in subsection 3.4.

3.3 THE ROLLOFF FUNCTION

From Eq. (3-3), it is seen that the power level P_r of the back-scattered signal depends on the backscattering coefficient σ^o, the distance R from the scatterometer to the surface area of interest, and the gains of the transmit and receive antennae. σ^o is generally observed to decrease with the angle of incidence θ over either land or water. And $R = h/\cos\theta$, h being the aircraft altitude, increases with θ. Since P_r is proportional to σ^o and inversely proportional to the fourth power of R, P_r is expected to decrease rapidly with θ. Moreover, the antenna pattern studied in the next section shows a decrease in two-way gain with increasing θ. This further enhance the decrease of P_r with θ. The rapid decrease of P_r with θ has an important bearing on the design and performance of the 13.3 GHz scatterometer system. For example, the signal noise ratio of the

Minicom 110 Tape Recorder System described in subsection 2.5 is limited to a maximum of 40 dB. If P_r at $\theta = 5^o$ is 40 dB or more higher than that at $\theta = 60^o$, then the signal power level would be either saturated at $\theta = 5^o$ or buried in the noise at $\theta = 60^o$ during data recording. Therefore, it is necessary to install certain filters to offset the strong dependence of P_r on θ.

To reduce the power level of the signal return at small θ before being recorded by the tape recorder, two rolloff filters were installed in each of two receiver data channels. One of the filters was used for observations over lands and the other over waters. Either one of the two filters is made operational by a control switch. The responses of these filters as a function of frequency for both receiver channels were measured in the laboratory at Building 15 of JSC and given in Table A-2 of Appendix A. The frequencies at which the filter responses were measured can be converted to the angles of incidence through Doppler relation of Eq. (3-4) for a given aircraft speed. The listed numbers in Table A-2 are average values of measurements on both data channels at each of the frequencies indicated. These numbers were plotted as a function of frequency in Figure 3-3 for both land and water filters. The values at the frequencies corresponding to $\theta \approx 5^o$, 10^o, 15^o, 20^o, 30^o, 40^o, 50^o and 60^o are obtained from these curves and used in the numerical calculation in Section 5.

As an example in the application of the rolloff functions $Z_\omega(\theta)$ and $Z\ell(\theta)$ given in Figure 3-3, observe that the values of σ^o over

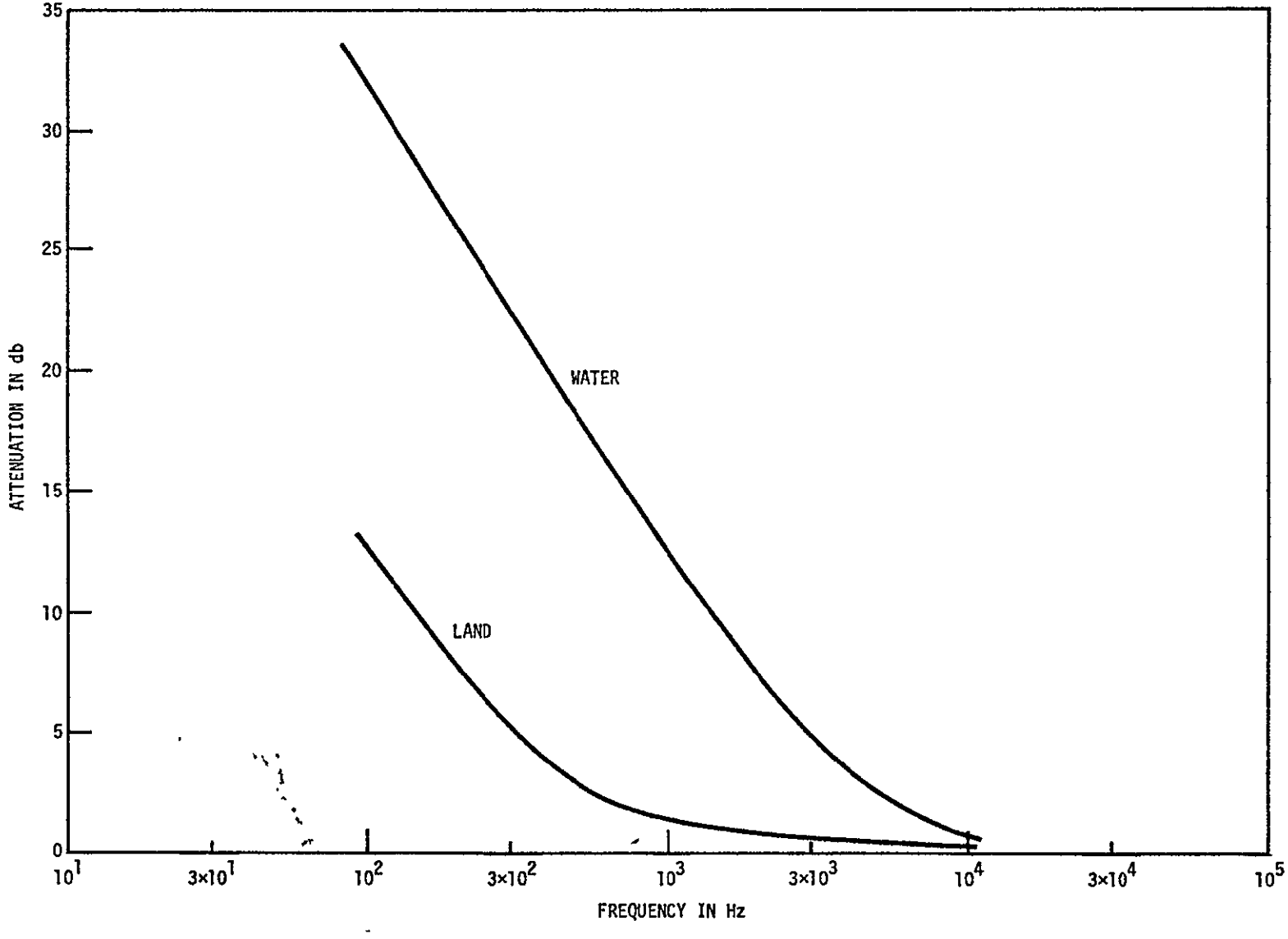

Figure 3-3.— The 13.3 GHz scatterometer rolloff functions.

calm water as obtained from Figure 3-4 in subsection 3.5 are ~ 18 dB and ~ -23 dB for $\theta = 5^{\circ}$ and $\theta = 60^{\circ}$, respectively. Assuming that the aircraft is cruising with a speed of ~ 75 m/sec and at an altitude of ~ 480 m, the Doppler frequencies are 580 Hz and 5760 Hz, and the distances are ~ 482 m and ~ 960 m for $\theta = 5^{\circ}$ and $\theta = 60^{\circ}$, respectively. The corresponding attenuations at these two frequencies are found from Figure 3-4 to be ~ 18 dB and ~ 1.8 dB. If area $A = 1\ m^2$, $P_t = 1$ watt, and neglecting the signal losses and amplifications in the scatterometer system, the receiver output powers at $\theta = 5^{\circ}$ and $\theta = 60^{\circ}$ were calculated from Eq. (3-3) and given in Table 3-1. It is clear from the table that there is a 48 dB difference in the signal returns at $\theta = 5^{\circ}$ and $\theta = 60^{\circ}$, which is more than the dynamic range of a typical tape recorder.

Therefore, on some mission over an extremely calm water surface, if the scatterometer variable gain amplifier is set to receive the backscattered signal return at $\theta = 5^{\circ}$ without saturation, then the signal return at $\theta = 60^{\circ}$ would be lower than the tape recorder noise.

It was found out from many observations over lands that the use of water rolloff filters generally yielded better results for the 13.3 GHz scatterometer. Therefore, it is reasonable to assume that the water rolloff filters will be most frequently used in the future missions either over land or over water. Only the water rolloff function $Z_{\omega}(\theta)$ will be used in the numerical calculations in section 5.

TABLE 3-1. - A NUMERICAL EXAMPLE OF THE BACKSCATTERED SIGNAL LEVELS AT THE RECEIVER OUTPUT

Parameters From Eq. (3-13)	$\Theta = 5^{o}$ $f_d = 70$ Hz	$\Theta = 60^{o}$ $f_d = 693$ Hz
P_t	1 Watt, 30 dBM	1 Watt, 30 dBM
$G_t G_r$	37 dB	27 dB
σ^o	18 dB	-23 dB
λ^2	$5 \times 10^{-4} m^2$, -32.9 dB	$5 \times 10^{-4} m^2$, -32.9 dB
$(4\pi)^3$	33 dB	33 dB
R^4	$5.35 \times 10^{10} m^4$, 107.3 dB	$8.46 \times 10^{11} m^4$, 119.3 dB
A	$1 m^2$, 0 dB	$1 m^2$, 0 dB
$Z_\omega(\Theta)$	17 dB	1.8 dB
$P_r(\Theta)$	-105 dBM	-153 dBM

3.4 THE MEASURED SYSTEM PARAMETERS

From the results of discussions in the previous three subsections, it is now possible to put all the parameters together and derive the final forms of the data processing equations. Note that both the backscattered and the calibrate signals, E_a and E_c in Equations (3-21b) and (3-22), pass through the water rolloff filters in the receiver data channels and, therefore, subject to the attenuations of the filters amounting to $Z_\omega(f)$ (or $Z_\omega(\theta)$). E_c occurs at the frequency of 12 KHz so that the value of Z_ω is ~ 0 dB. Consequently, only the $Z_\omega(f)$ for E_a needs to be taken into account and Eq. (3-24) should be rewritten as

$$W_{ra}(f_d) = P_t Z_\omega(f_d) \left(\frac{E_a}{E_c}\right)^2 \frac{1}{K} \tag{3-25}$$

Combining Equations (3-6), (3-7), and (3-25), the expression for the first form of the data processing equations becomes

$$\frac{Z_\omega(f_d)}{K} \left(\frac{E_a}{E_c}\right)^2 \Delta f_d = \frac{\lambda^2}{(4\pi)^3} \sum_{i=1}^{N} \frac{G_t(\theta_i)\, G_r(\theta_i)\, \sigma^o(\theta_i)}{R^4(\theta_i)} \Delta A_i \tag{3-26}$$

Similarly, the second form of the data processing equations is obtained by combining Equations (3-11) and (3-25). The result is

$$\sigma^o(\theta) = \frac{(4\pi)^3\, 2Vh^2 Z_\omega(\theta)}{K G_t(\theta) G_r(\theta) \lambda^3 \Delta\phi} \left(\frac{E_a}{E_c}\right)^2 \tag{3-27}$$

Note that, in Eq. (3-26), $E_a^2 \Delta f_d$ is the relative receiver output power in the Doppler frequency band Δf_d corresponding to the signal return from the ground cell defined by two isodopplers, $f_d + \frac{1}{2}\Delta f_d$ and $f_d - \frac{1}{2}\Delta f_d$.

Two key system parameters were measured in Building 15 of JSC, namely, K, and $Z_\omega(\theta)$. The results of the recent measurements of these parameters were given in Appendix A. The rolloff filters were permanently installed in the scatterometer system. Consequently, the values of $Z_\omega(\theta)$, which were presented in the previous section, are not expected to change much from measurements at different times unless the filters were replaced. The values of K, on the other hand, could change for different missions. The parameter K controls the power level of the calibrate signal which is also subject to the limitation of the tape recorder dynamic range. For a given surface of backscattering and aircraft altitude, K could be adjusted for an appropriate calibrate signal level to bring about the best signal to noise ratio for the data. The values of K measured for Mission 347 functional check flight as presented in Appendix A will be used for the numerical calculations in section 5.

3.5 THE FUNCTIONAL DEPENDENCE OF L-BAND σ^o ON θ

It was pointed out previously that the ordinary approach of deriving the backscattering coefficient σ^o, by means of a Doppler radar such as the 13.3 GHz scatterometer, is to use the second form of the data processing equation given by Eq. (3-27). The σ^o derived

from this approach contains two sources of error, both resulting from the approximation of a rectangular area (Figure 3-2) for an actual doppler cell defined by two isodopplers (Figure 3-1). The first source of error comes from the assignment of a single value of σ^o for a given rectangular ground cell. Actually, σ^o was observed to vary with incident angle θ, and the contribution to the observed signal return within a given bandwidth Δf_d is the sum of the backscattered signals from all the small area elements with different θ_i's in the doppler cell.

The second source of error is due to the crudeness of the area approximation itself. Both of the error sources depend on the scatterometer antenna beamwidth. It is desirable to explore the amount of error introduced in the σ^o derivation by using the second form of data processing equation. The σ^o derived from the first form of data processing equation given by Eq. (3-26) provide an adequate standard for comparison.

The derivation of σ^o by Eq. (3-26) requires an assumed functional dependence of σ^o on θ to begin with, as pointed out previously. To see how the shape of σ^o versus θ curve affects the error in the σ^o estimation by Eq. (3-27), the measured values of σ^o from both smooth and rough surfaces of backscattering are considered. For the smooth surface, the measurements made in February 1971 over North Atlantic Ocean site 166 (mission 156) and reported by Krishen et. al. (ref. 7) are adopted. For the rough surface, the measurements made over a test site near Garden City, Kansas in

June 1970 (mission 133) and reported by Dickey et. al. (ref. 5) are used. The results from both of these measurements are shown in Figure 3-4. The land data shown in the figure (X sign) were derived from the smooth curve on Figure 4 of Dickey et. al. (ref. 5).

The data over the calm sea showed a power law dependence of σ^o on θ. As displayed in Figure 3-4, the measured σ^o dependence on θ was well represented by the relation:

$$\sigma^o = 163.2\theta^{-0.76} - 30.0 \qquad (3\text{-}28)$$

A quadratic regression was performed on the data from the measurements over land. The result is given by:

$$\sigma^o = 0.0027\theta^2 - 0.3533\theta + 6.101 \qquad (3\text{-}29)$$

In both of the above equations, the unit of σ^o is in dB and that of θ in degree. Both of these expressions are used in the numerical calculations in subsection 5.2, where the two forms of the data processing equations are compared.

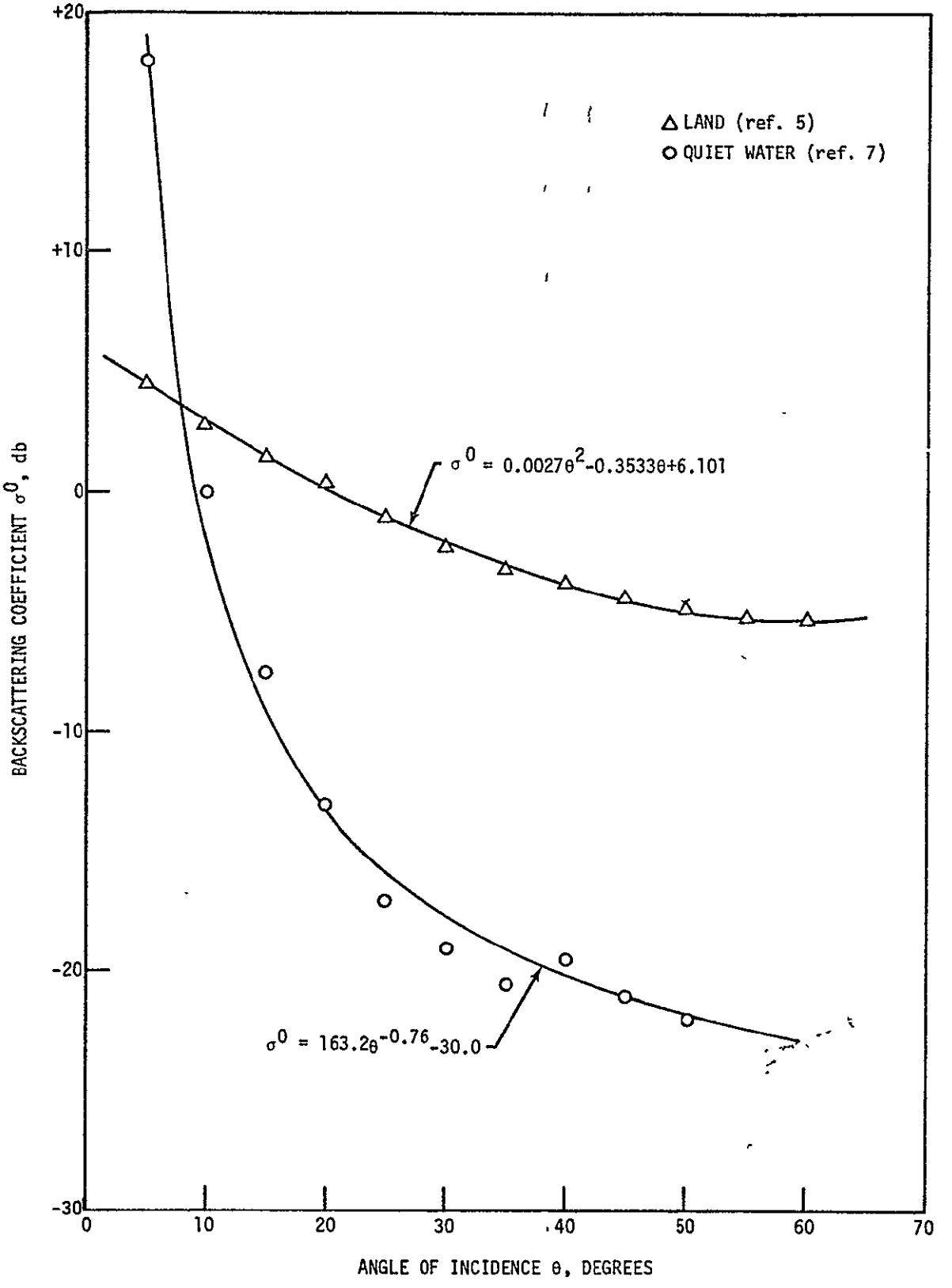

Figure 3-4.— The functional dependence of Σ° on θ.

4. THE ANTENNA PATTERN

4.1 THE MAIN BEAM GAIN

The most recent measurements of the gain patterns for both transmit and receive antennae of the 13.3 GHz scatterometer were carried out in 1976 in Bldg. 14 of JSC. The measurements were made for every 1° interval in both along-track and cross-track directions. Since it was known from the previous experience that the side-lobe gain (two-way) was ~30 dB or more below the main beam gain for these antennae, the gain patterns were measured only over $\pm 10^{\circ}$ in the cross-track direction. The measurements were performed with mock-up to simulate the effect of the aircraft body. Consequently, the measured gain patterns are expected to be close to reality.

To see the spatial variation of the antenna patterns, the contour maps of the one-way gains are displayed in Figure 4-1 and 4-2 for the transmit and receive antennae respectively. Each of the maps covers the angular ranges of ϕ from $\sim -10^{\circ}$ to $\sim +10^{\circ}$ and of θ from -70° to $+70^{\circ}$. The direction of the nadir is located at $\theta = 0$ and $\phi = 0$. From these figures it is clear that both antennae show a narrow beamwidth of $\sim 3^{\circ}$ and three gain maxima within θ range of $\pm 40^{\circ}$. The gain maxima of both antennae occur at $\theta = \sim -25^{\circ}$, $\sim 0^{\circ}$, and $\sim +25^{\circ}$. Although the gain pattern measurements were limited to within $\phi = \pm 10^{\circ}$, the data plotted in Figure 4-2 indicated a side-lobe level some 20 dB or more below that of the main beam.

Figure 4-3 shows the variations of the antenna two-way gain with θ for $\phi = 0$, -1° and $+1^{\circ}$. The two-way gain maxima at $\theta = 0^{\circ}$ and

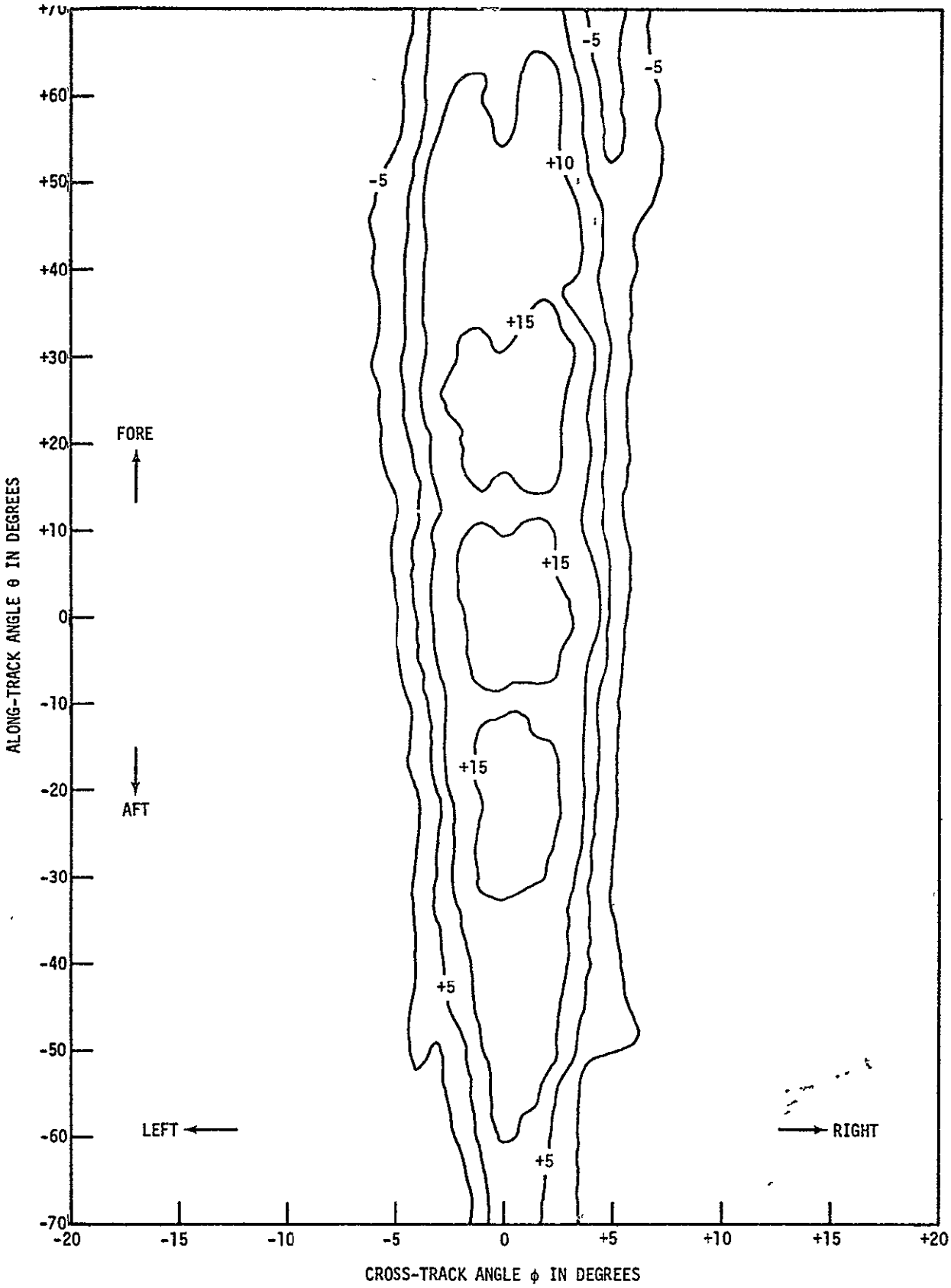

Figure 4-1.— The one-way gain contour of the 13.3 GHz scatterometer vertical receive antenna.

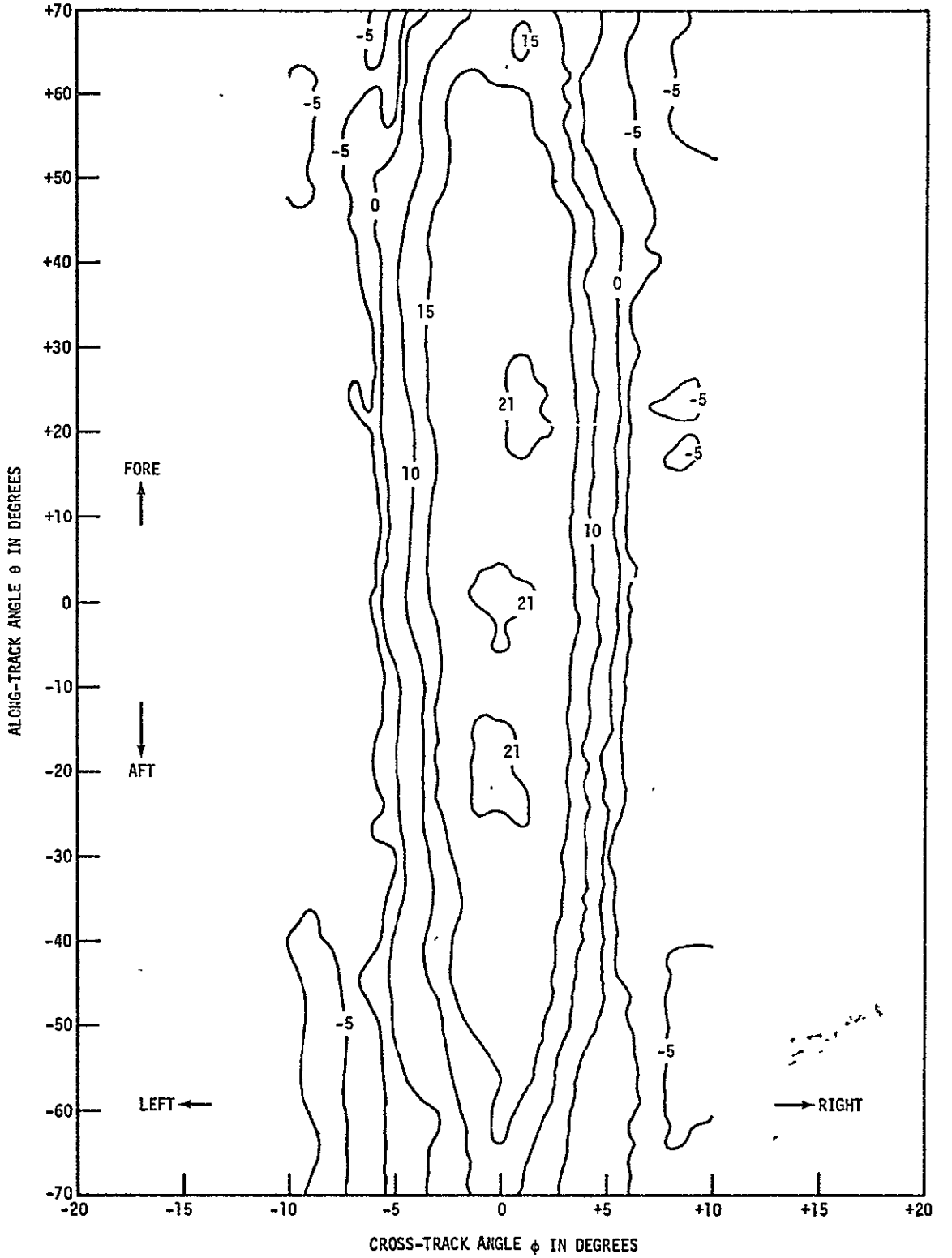

Figure 4-2.— The one-way gain contour of the 13.3 GHz scatterometer vertical transmit antenna.

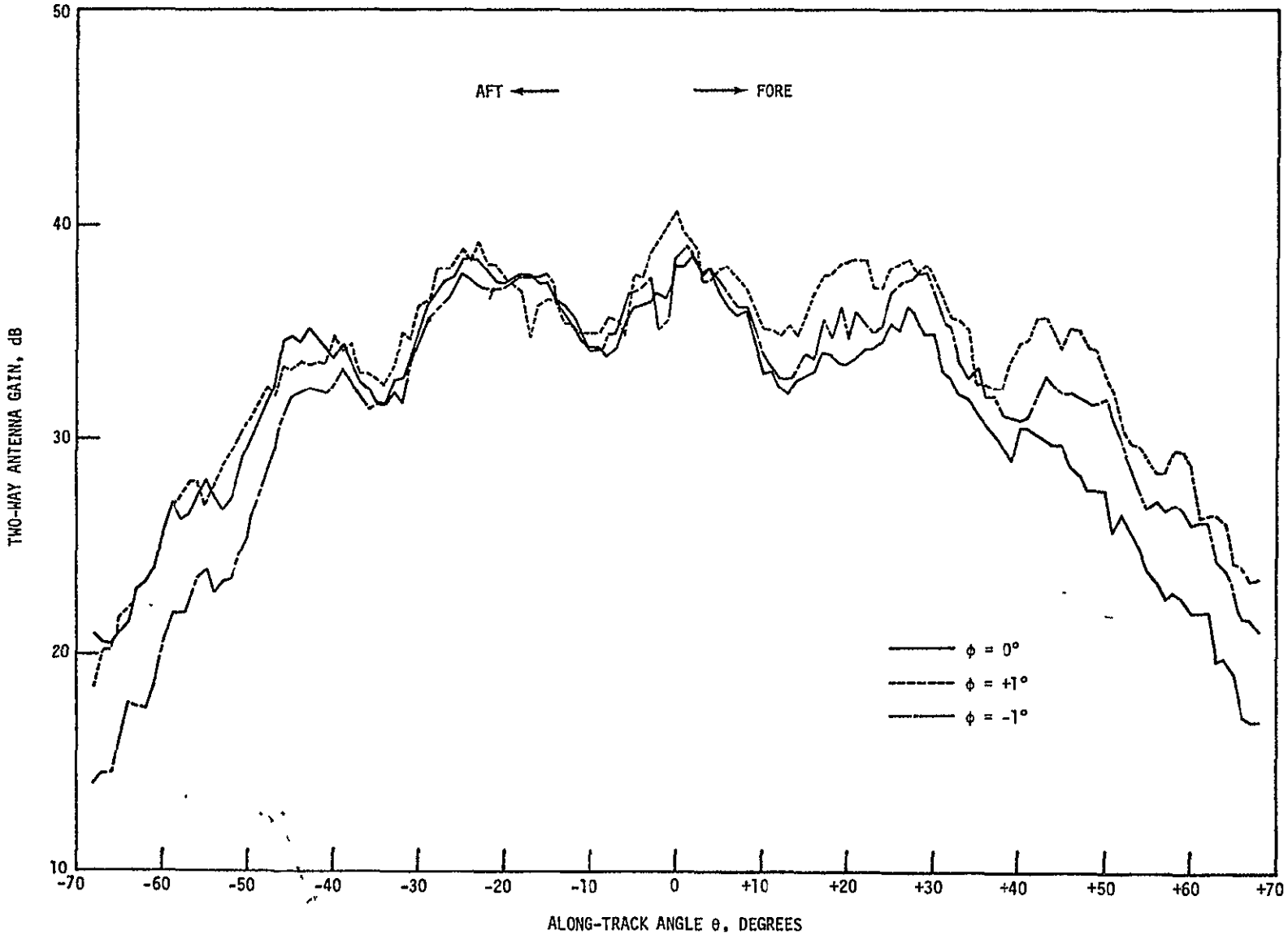

Figure 4-3.— The antenna gain variation with incident angle.

$\theta \sim \pm 25^{o}$ are comparable at 36-39 dB. Additional gain maxima of smaller magnitudes ($\sim$31-35 dB) are also present at $\theta \sim \pm 45^{o}$. Beyond $\theta = \pm 50^{o}$, the two-way gain decreases rapidly. Another feature displayed by these curves is the asymmetry of the gain in the fore and the aft directions. For any θ in the fore direction, the gain at $\phi = 0^{o}$ is smaller than those at $\phi = \pm 1^{o}$. This implies a double main beam maxima in the cross-track gain profile which will be discussed in more detail in the next few subsections.

To see the beamwidth variation with θ, the same approach used in the analysis of the 1.6 GHz scatterometer system (ref. 11) is adopted here. Two methods of estimating the antenna beamwidth are defined. The first one is to take the maximum value of the two-way gain $G_o^2 F(\theta)$ at an incident angle θ. A 3-dB value was subtracted from $G_o^2 F(\theta)$ (in dB). Two values of the cross-track angles ϕ_1 and ϕ_2, measured from the location of $G_o^2 F(\theta)$, were determined where the antenna gain equaled $G_o^2 F(\theta)$ - 3 dB. The 3-dB beamwidth is the sum of ϕ_1 and ϕ_2. The second method (summation method) of defining a beamwidth is given by

$$\Delta\phi(\theta) = \frac{\int_{\phi_1}^{\phi_2} G_t(\theta,\phi) G_r(\theta,\phi) d\phi}{G_o^2 F(\theta)} \qquad (4\text{-}1)$$

where ϕ_1 and ϕ_2 are the cross-track angles where the null points of the main-beam antenna two-way gain occur. $G_t(\theta,\phi)$ and $G_r(\theta,\phi)$ are the one-way gain at location defined by θ and ϕ of the transmit and receive antennae respectively. All the gains in Eq. (4-1) are expressed in numerical value (not in dB). The results from those

two methods of beamwidth definition are shown in Figure 4-4. The dotted and solid curves in this figure give the beamwidth ($\Delta\phi$) variation with θ as determined by 3-dB and summation methods respectively.

Clearly, there is an asymmetry in the variation of $\Delta\phi$ with θ in the fore and aft directions. In the aft direction, $\Delta\phi$ decreases from $\sim 4^{o}$ at $\theta=-5^{o}$ to $\sim 2.4^{o}$ at $\theta=-65^{o}$. Throughout the θ range from -5^{o} to -70^{o}, the $\Delta\phi$'s determined by these two methods track each other very well, the difference between them being not more than $\sim 0.3^{o}$. On the other hand, $\Delta\phi$'s in the fore beam vary about a mean value of $\sim 4^{o}$. The range of variation is from 3^{o} to 5^{o} and from 2.1^{o} to 5.7^{o} for $\Delta\phi$ determined by summation method and 3-dB method respectively. The reason for large variation in $\Delta\phi$ determined by 3-dB method is due to the double maxima in the cross-track gain profile mentioned previously. For large $\Delta\phi$, the values of the two gain maxima differ by less than 3dB so that the locations of both maxima are contained within $\Delta\phi$. For small $\Delta\phi$, the difference in the two maximum gains is more than 3 dB so that only the larger gain peak is contained in $\Delta\phi$.

From the above discussion, it is clear that special care must be taken in the derivation of the backscattering coefficient σ^{o} from the data obtained in the fore beam. The beamwidth $\Delta\phi$ determined by 3-dB method could result in an appreciable error in the σ^{o} calculation. The $\Delta\phi$ determined by the summation method will be used in the numerical calculation presented in Section 5.

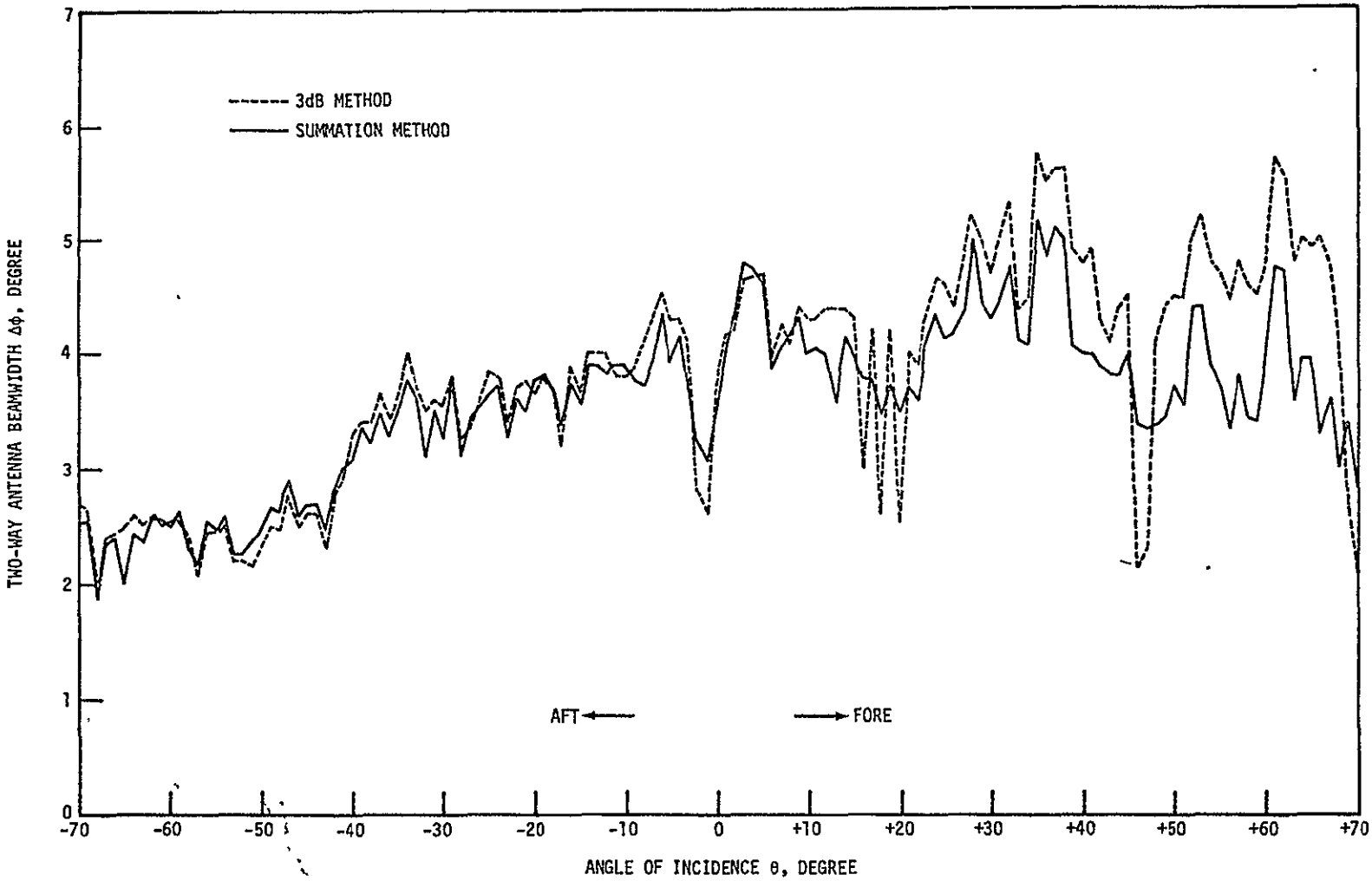

Figure 4-4.— The antenna beamwidth variations with incident angle.

4.2 THE SIDE LOBE LEVEL

Since the antenna gain measurements were made only in the region within $\phi = \pm 10^{o}$, not many side lobes were observed in the measured data. Figures 4-5 and 4-6 showed, from the limited data, the cross-track gain profiles at two selected incident angles in aft and fore directions respectively. For $\theta = -10^{o}$ and $\theta = -60^{o}$ in Figure 4-5, the side lobe gains are down by ~55 dB and ~33 dB, respectively, compared to the main beam gains. In figure 4-6, the side lobe gain at $\theta = 60^{o}$ is again down by ~33 dB compared to the main beam gain. At $\theta = 10^{o}$, there is difficulty in determining the side lobe level. However, from the past experiences (S. C. Reid, personal communication), the side-lobe gain at that incident angle is at least 50 dB below the main beam gain. The side lobe gain at other incident angles were also examined and were found to be at least ~30 dB below the main beam gain maxima.

It is noted that the antenna parameters $G_t(\theta)$, $G_r(\theta)$ and $\Delta\phi(\theta)$ appear together in the denominator of the data processing equation (3-27). To give a crude estimate on the side-lobe contribution to the total input receiver signal, it is necessary to compare the relative values of the product $G_o^2 F_i(\theta)\Delta\phi_i(\theta)$ (antenna gain factor, subscript i refers to either side lobes or main beam) for the side lobes and their associated main beam. For example, the beamwidth of the main beam at $\theta = -60^{o}$ is ~2.5^{o} which together with the two-way gain plot shown in Figure 4-5 results in an antenna gain factor of ~13 dB. The beamwidth of the first side lobe at $\theta = -4^{o}$ is ~1.8^{o} which combines with a two-way gain of ~-10 dB gives an

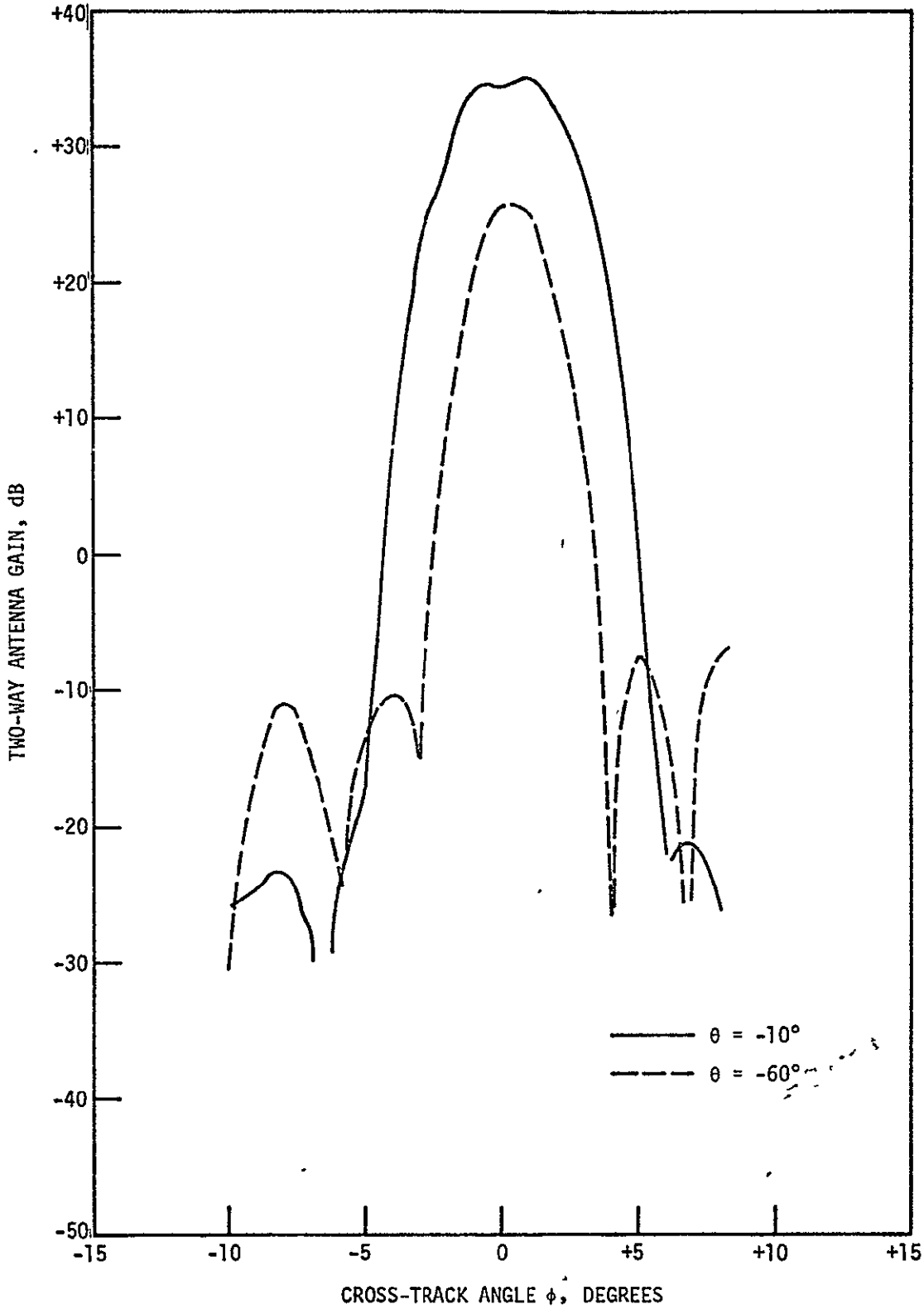

Figure 4-5.— The cross-track two-way antenna gain profile.

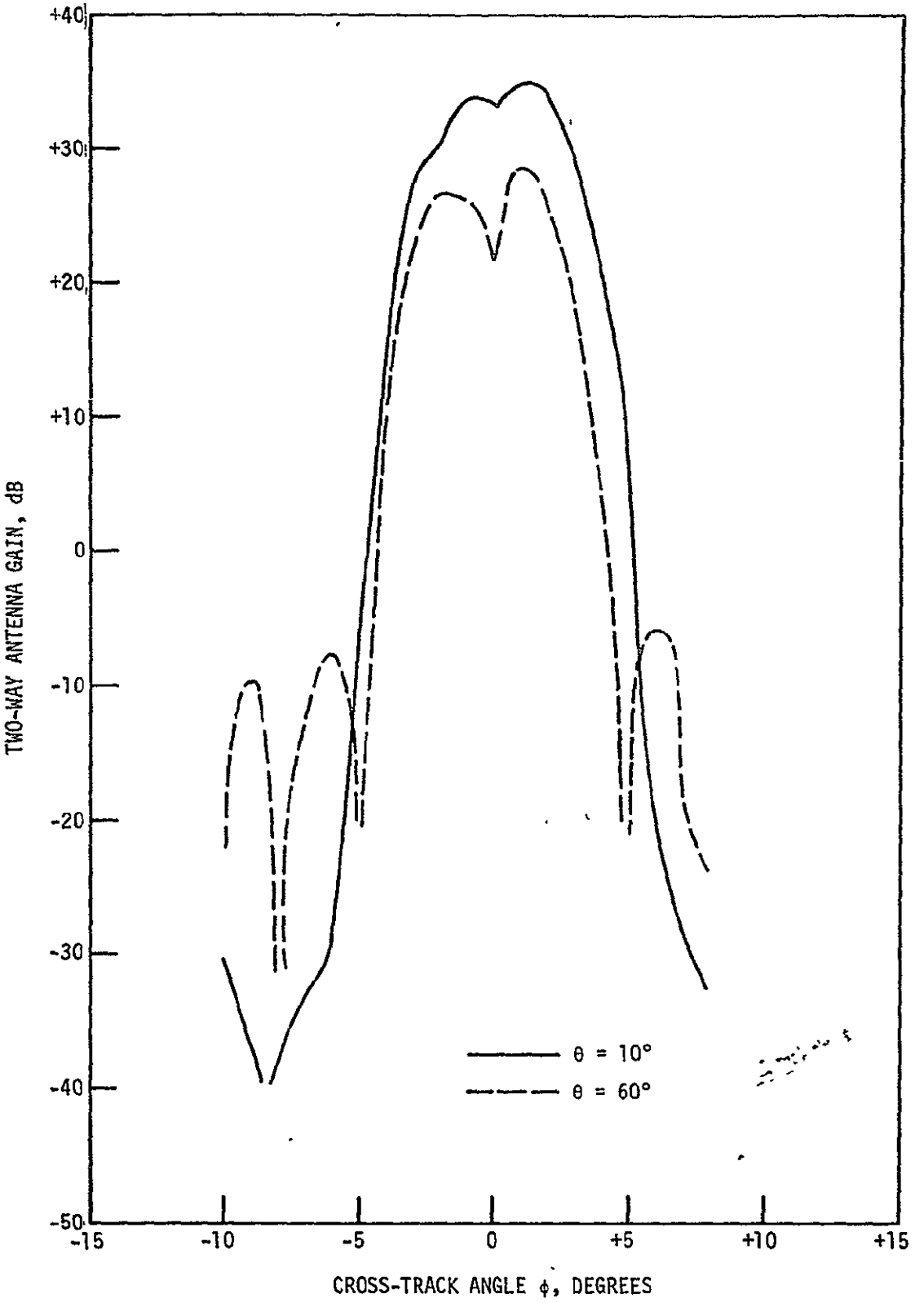

Figure 4-6.— The cross-track two-way antenna gain profile.

antenna gain factor of ~-25 dB. Assuming that the side lobes are separated by ~4° and are of the same peak gain of ~-10 dB each, the total side-lobe contribution over the entire range of ϕ from ±5° to ±90° is about -8.7 dB, which is ~21.7 dB smaller than the main beam antenna gain factor. It can be shown that at other θ's, the total side-lobe contribution to the main beam signal is at least ~20 dB down and is totally negligible.

Figure 4-5 also shows the more than 1° difference in beamwidth between the small and large incident angles in the aft beam. And Figure 4-6 displays the double maxima in the cross-track gain profile in the fore beam as described in the previous subsection.

4.3 THE ANTENNA CROSS POLARIZATION

The antenna response to the cross-polarized RF waves at the same frequency of 13.3 GHz was not included in the most recent measurements of the gain pattern. The effect of the antenna cross-polarization response was found to introduce some error in the estimate of the cross-polarized backscattering coefficients σ^{o}_{HV} and σ^{o}_{VH} for the 1.6 GHz scatterometer system; for the linear-polarized backscattering coefficients σ^{o}_{HH} and σ^{o}_{VV} the effect was negligible. Since the 13.3 GHz scatterometer provides the estimate of σ^{o}_{VV} only, it is expected that the error introduced by this effect should be small. To give a crude estimate of this effect, the measurements of the cross-polarized response made in 1969 were examined here. Figures 4-7 and 4-8 showed the measured cross-polarized gains as a function of θ for the transmit antenna.

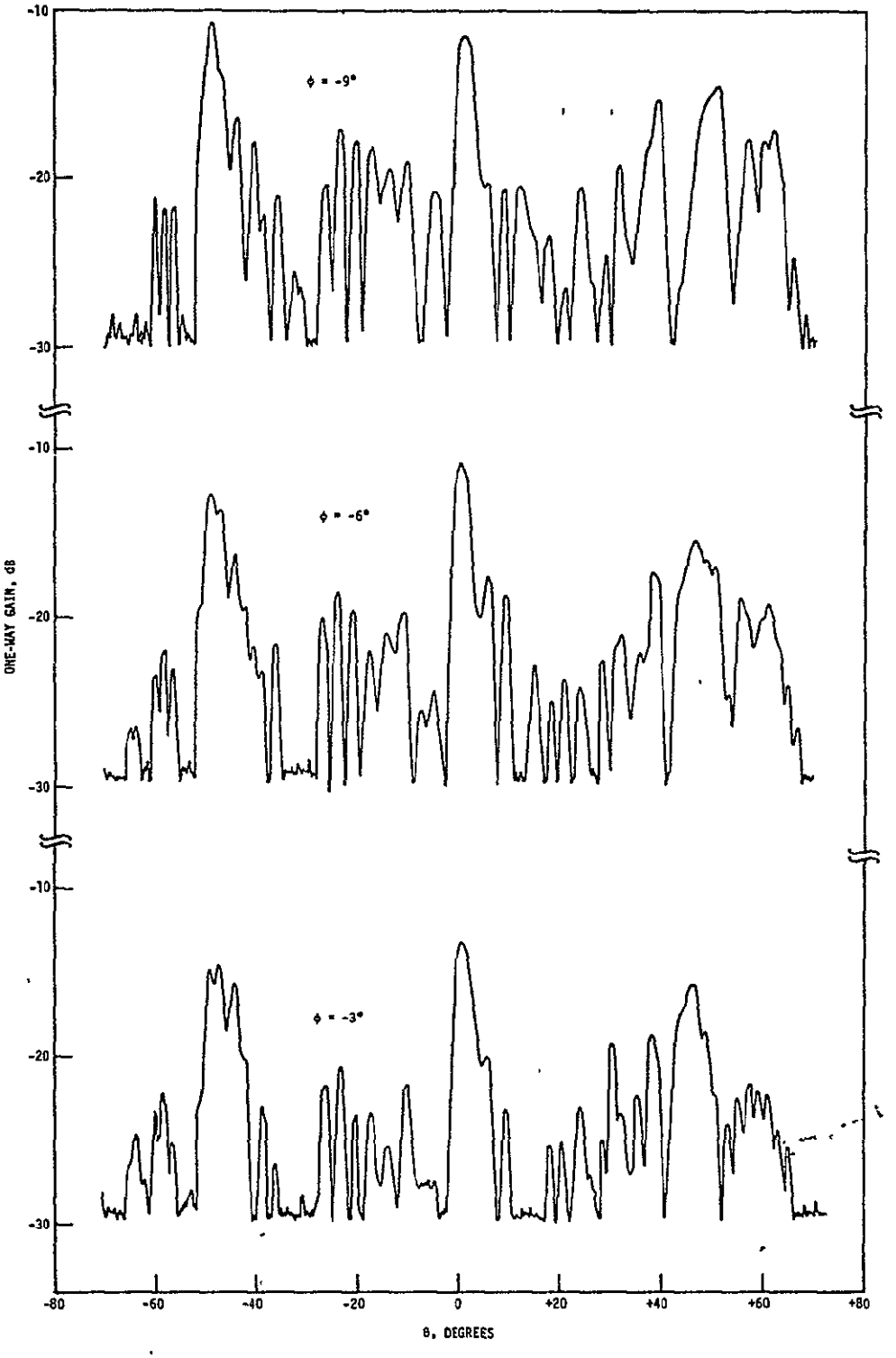

Figure 4-7.— The cross-polarized gain of the vertical tranmit antenna.

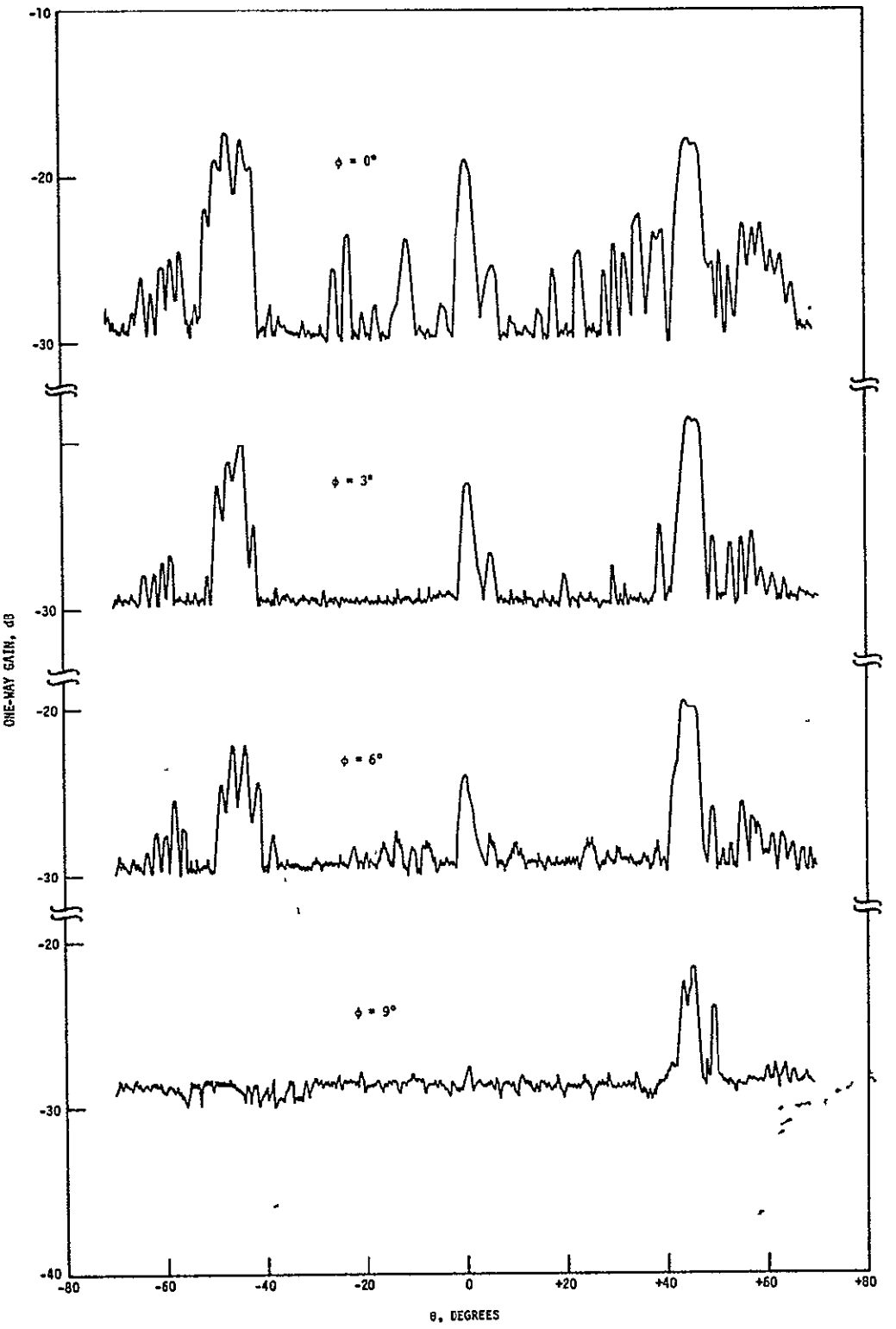

Figure 4-8.— The cross-polarized gain of the vertical transmit antenna.

Figure 4-9 and 4-10 displayed the same type of data for the receive antenna. The measurements were made at a cross-track angular interval of 3^{o}. The plots in Figures 4-7 and 4-8 showed that the high cross-polarization gains occured at $\theta \approx 0^{o}$, $\pm 45^{o}$ for all ϕ and that higher gains were observed for $\phi \lesssim 0^{o}$ than for $\phi > 0^{o}$. The observed gain values were less than -10 dB. The cross-polarized gain plots for the receive antenna in Figures 4-9 and 4-10, on the other hand, showed the higher gain for $\phi \geq 0^{o}$ than for $\phi < 0^{o}$. All of the observed gain values were less than -15 dB. The prominant cross-polarized gain peaks occured at $0 \approx 0^{o}$, $\pm 45^{o}$ and $\pm 55^{o}$ for this antenna.

The effect of the antenna cross-polarization response is to make undesirable contribution to the total receiver signal input. Including this cross-polarization effect, the receiver input power should be modified and expressed by

$$P_{rvv}(\theta) = \frac{\lambda^2 P_t \Delta A(\theta)}{(4\pi)^3 R^4(\theta)} \left[G_{tvm}(\theta)\sigma^{o}_{vv}(\theta)G_{rvm}(\theta) + G_{tvc}(\theta)\sigma^{o}_{hv}(\theta)G_{rvm}(\theta) \right.$$

$$\left. + G_{tvm}(\theta)\sigma^{o}_{vh}(\theta)G_{rvc}(\theta) + G_{tvc}(\theta)\sigma^{o}_{hh}(\theta)G_{rvc}(\theta) \right] \qquad (4\text{-}2)$$

where

$\Delta A(\theta)$ = the area of the ground cell at incident angle θ.

$G_{tvm}(\theta)$ = vertically-polarized gain of the transmit antenna at θ.

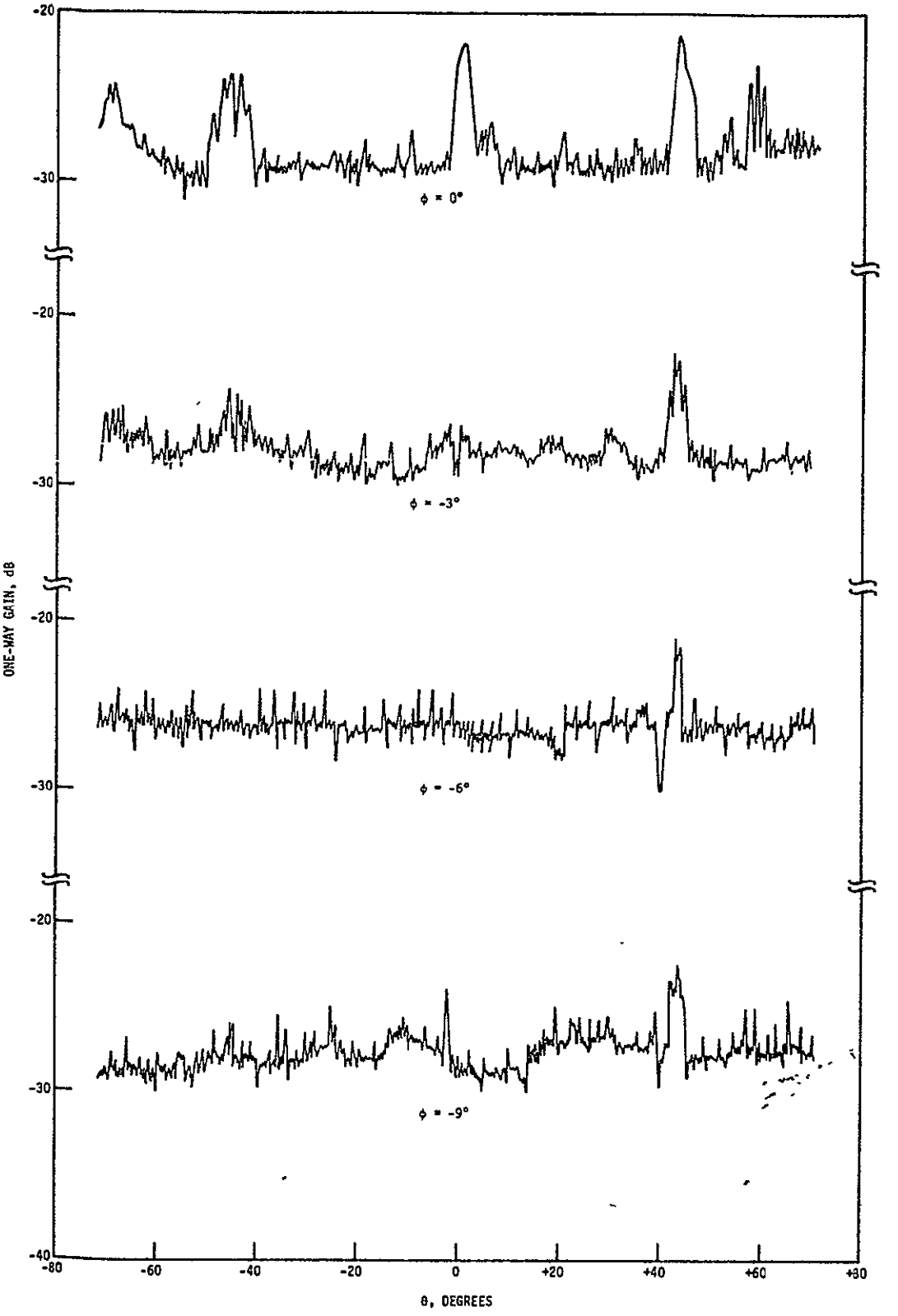

Figure 4-9.— The cross-polarized gain of the vertical receive antenna.

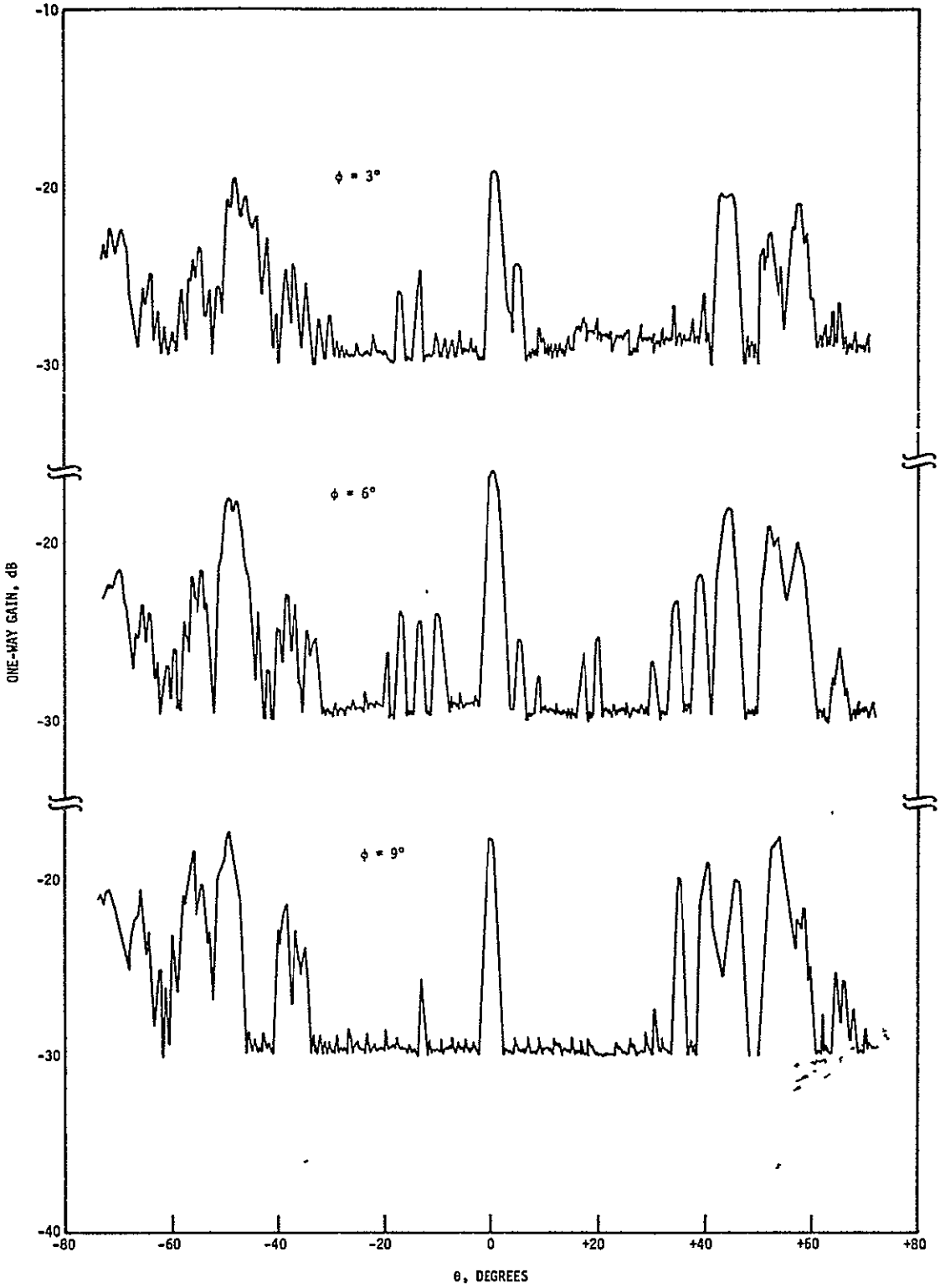

Figure 4-10.— The cross-polarized gain of the vertical receive antenna.

$G_{tvc}(\theta)$ = cross-polarized gain of the transmit antenna at θ.

$G_{rvm}(\theta)$ = vertically-polarized gain of the receive antenna at θ.

$G_{rvc}(\theta)$ = cross-polarized gain of the receive antenna at θ.

The remaining symbols in Eq. (4-2) were defined previously. The first term inside the bracket in the above equation is the dominant term which represents the backscattered signal of interest. The three remaining terms are contributions of the undesirable signals due to antenna cross-polarization effect. These three terms, in sequential order, represent:

- The return signal at the receiver due to the signal transmitted in cross polarization by the transmit antenna and backscattered in vertical polarization.

- The return signal at the receiver due to the signal transmitted in vertical polarization by the transmit antenna and backscattered in horizontal polorization.

- The return signal at the receiver due to the signal transmitted in cross polarization by the transmit antenna and backscattered in horizontal polarization.

Based on Figures 4-7, 4-8, 4-9 and 4-10, and the main beam antenna gain patterns, the relative contributions to the total power return of four terms in Eq. (4-2) can be estimated at some selected locations. The results of these estimates at six chosen

locations, where prominent cross-polarized gains were observed, were given in Table 4.1. The estimates were made with respect to the product of the two-way gain and σ^o. It is clear from this table that, without considering the relative values of all the σ^o's, the signal of interest as represented by $G_{tvm}\sigma^o_{vv}G_{rvm}$ is about 20 dB or more greater than the three undesirable signal contributions due to antenna cross-polarization effect. σ^o_{vv} is generally comparable to σ^o_{hh} and is at least a few dB greater than σ^o_{hv} and σ^o_{vh}. This tends to make the undesirable signal contributions even more insignificant. Although the estimates were only made at six locations, it is quite clear that, if the backscattered signals were integrated over a ground cell as was done in the 1.6 GHz scatterometer system study (ref. 11), the contributions due to antenna cross-polarization response would be totally negligible.

4.4 THE VARIATION OF ANTENNA GAIN FACTOR WITH θ

It was noted previously that the antenna gain $G_o^2F(\theta)$ and beam-width $\Delta\phi(\theta)$ appeared together in the denominator of Eq. (3-27). This combined antenna gain factor directly affects the σ^o estimate that its variation with θ should be examined in more detail. Figure 4-11 shows the dependence of this factor on θ in both fore and aft directions. It is seen from this curve that there are six or seven ripples in the θ range from -60^o to $+60^o$. The existence of these ripples would require accurate determination of θ during data processing. For example, if the error in the pitch angle correction is $\sim 1^o$, then the error in σ^o at some θ's could be as large as ~1 dB.

TABLE 4-1. - THE RELATIVE POWER CONTRIBUTIONS TO THE TOTAL BACKSCATTERED SIGNAL (dB)

Along-Track Angle θ, Degrees	Terms	Cross-Track Angle ϕ, Degrees		
		0	+3	-3
+45	$G_{tvm}G_{rvm}\sigma^o_{vv}$	σ^o_{vv} + 29.7	σ^o_{vv} + 29.7	σ^o_{vv} + 29.8
	$G_{tvc}G_{rvm}\sigma^o_{hv}$	σ^o_{hv} - 0.8	σ^o_{hv} - 1.3	σ^o_{hv} + 0.9
	$G_{tvm}G_{rvc}\sigma^o_{vh}$	σ^o_{vh} - 8.1	σ^o_{vh} - 7.8	σ^o_{vh} - 9.2
	$G_{tvc}G_{rvc}\sigma^o_{hh}$	σ^o_{hh} - 39.0	σ^o_{hh} -39.1	σ^o_{hh} - 38.4
-45	$G_{tvm}G_{rvm}\sigma^o_{vv}$	σ^o_{vv} + 34.7	σ^o_{vv} + 21.9	σ^o_{vv} + 14.1
	$G_{tvc}G_{rvm}\sigma^o_{hv}$	σ^o_{hv} + 1.9	σ^o_{hv} - 7.0	σ^o_{hv} - 5.5
	$G_{tvm}G_{rvc}\sigma^o_{vh}$	σ^o_{vh} - 9.0	σ^o_{vh} - 11.5	σ^o_{vh} - 21.7
	$G_{tvc}G_{rvc}\sigma^o_{hh}$	σ^o_{hh} - 41.6	σ^o_{hh} - 42.0	σ^o_{hh} - 41.2

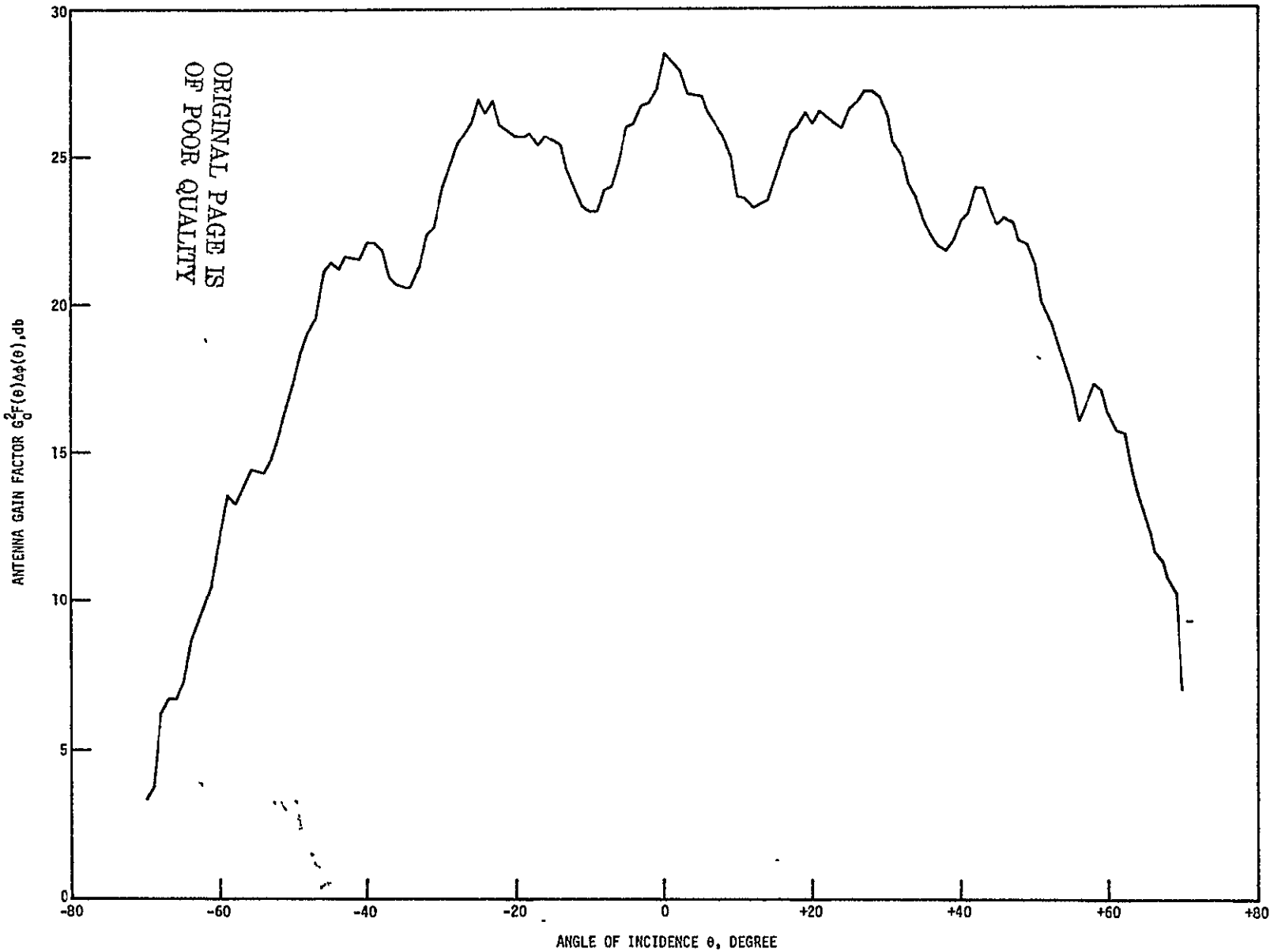

Figure 4-11.— The variation of the antenna gain factor with θ.

The rapid variation of $G_o^2 F(\theta)\Delta\phi(\theta)$ with θ also requires that the mounting of the antennae onto the aircraft should conform to the laboratory mounting when the gain patterns were measured. Another words, the coordinate system in the laboratory gain measurements should be precisely the same as the aircraft coordinate system. If imprecision exists in the antenna mounting either in the laboratory or the aircraft, error would result in the σ^o estimate which, if large enough, would make the interpretation of the backscattering phenomena difficult.

5. NUMERICAL RESULTS AND DISCUSSION

5.1 THE COMPUTER PROGRAM

The numerical calculations of the receiver signal outputs were performed according to Eq. (3-26). The area elements used in the numerical integration covered 1^{o} in ϕ. The centers of the area elements lie on the isodoppler corresponding to the along-track incident angle θ_o. The area element ΔA_i and distance R_i have to be expressed in terms of the measured θ and ϕ. The derivation of the expressions for these two parameters were given in Appendix D. The antenna gains $G_t(\theta_i)$ and $G_r(\theta_i)$, the backscattering coefficient $\sigma^{o}(\theta_i)$ and the distance $R(\theta_i)$ within the summation sign of Eq. (3-26) were all evaluated at the centers of ΔA_i's. When these centers did not fall on the positions where the actual measurements of $G_t(\theta_i)$ and $G_r(\theta_i)$ were made, linearly interpolated values from the immediate neighbors were used. The summation was carried out to the null points on both sides of the main beam.

The computer program was designed and implemented in accordance with Eq. (3-26). It evaluated the power outputs in terms of the square of the backscattered to calibrate signal voltage ratio, $\left(\frac{E_a}{E_c}\right)^2$. Eight angles of incidence at 5^{o}, 10^{o}, 15^{o}, 20^{o}, 30^{o}, 40^{o}, 50^{o}, and 60^{o} were chosen for the computations. Since the along-track cell length is a fixed value of 25m, the bandwidth Δf_d changes with angle of incidence, decreasing from 381 Hz at $\theta = 5^{o}$ to 48 Hz at $\theta = 60^{o}$. Eight values of rolloff functions $Z_w(f_d)$ corresponding to the eight incident angles are entered in the

program as a table. The value of the calibrate constant K was given in Appendix A and treated as a constant in the program. The effects of both the antenna cross-polarization response and the side lobe gain were already shown in Section 4 to be negligible in the receiver signal input. Thus, the computer program did not include the computations of these two undesirable signal contributions.

The program was coded in Fortran. It consisted of the main program and a subroutine. All of the computations leading to the values of $\left(\frac{E_a}{E_c}\right)^2$ for all selected incident angles were performed in the main program. The subroutine was used to obtain the values of the two-way antenna gain for the calculation of signal return, given the incident angle θ_o and cross-track angle ϕ_i. The two-way antenna gain pattern was previsouly saved on a magnetic tape and read and stored in the disk during the program run. The program listing and flow chart are given in Appendix D. The program was run on the UNIVAC 1110 computer at JSC.

5.2 THE σ^o DERIVATION

As pointed out in Section 3, it is necessary to assume a functional dependence of σ^o on the incident angle θ in the first method of σ^o deviation. This assumption was made according to Eqs. (3-28) and (3-29) for the backscattering from water and land, respectively. With this assumption the receiver signal outputs in terms of $\left(\frac{E_a}{E_c}\right)^2$ could be obtained by running the program listed in Appendix D. The signal outputs obtained in this way could be compared with those

actually obtained from observations to determine the validity of the assumed σ^o dependence on θ. The procedure is straightforward and will not be performed here. Instead, a comparison will be made between the first (as represented by Eq. (3-26)) and second (as represented by Eq. (3-27)) methods of σ^o derivation.

To do such a comparison, the values of $\left(\frac{E_a}{E_c}\right)^2$ resulted from the computer runs were taken to be the receiver output signals for both methods. Then the σ^o dependence on θ as derived from the first method will be given by Eq. (3-28) for water and Eq. (3-29) for land. The numerical values from these equations at the incident angles of $\pm5^o$, $\pm10^o$, $\pm15^o$, $\pm30^o$, $\pm40^o$, $\pm50^o$, and $\pm60^o$ were listed under the "σ_1^o" columns in Tables 5-1 and 5-2. Table 5-1 gave the σ^o values for the fore beam and Table 5-2 for the aft beam. σ^o's from both over water and over land were entered in these tables.

The corresponding values of the σ^o's derived from the second method of Eq. (3-27) were given in the same two tables under the "σ_2^o" columns. The same numerical values for the parameters such as altitudes, aircraft speed, cell length, and calibrate constant K were used in Eqs. (3-26) and (3-27). It is clear from these tables that, for observations over land where σ^o vs θ curve is not steep, the σ^o estimated from both methods are comparable for all θ selected for computation. For backscattering from smooth water surface, the estimated σ^o's from the two methods could differ appreciably for small incident angles, as can be seen from these two tables. For $|\theta| \geq 20^o$ where σ^o vs θ curve (see Figure 3-4) is

TABLE 5-1. - A COMPARISON OF σ^{o} VALUES (dB) DERIVED FROM TWO DIFFERENT APPROACHES - FORE BEAM

Angle of Incidence θ (Degrees)	Water		Land	
	σ_1^{o}	σ_2^{o}	σ_1^{o}	σ_2^{o}
5	18.03	15.78	4.40	4.27
10	-1.64	-2.08	2.84	2.78
15	-9.16	-9.32	1.41	1.38
20	-13.25	-13.33	0.12	0.09
30	-17.69	-17.73	-2.06	-2.09
40	-20.11	-20.12	-3.71	-3.72
50	-21.65	-21.73	-4.81	-4.89
60	-22.73	-22.76	-5.38	-5.40

TABLE 5-2. - A COMPARISON OF σ^{o} VALUES (dB DERIVED FROM TWO DIFFERENT APPROACHES - AFT BEAM

Angle of Incidence θ (Degrees)	Water		Land	
	σ_1^{o}	σ_2^{o}	σ_1^{o}	σ_2^{o}
-5	18.03	15.98	4.40	4.29
-10	-1.64	-1.99	2.84	2.79
-15	-9.16	-9.27	1.41	1.38
-20	-13.25	-13.30	0.12	0.10
-30	-17.69	-17.71	-2.06	-2.08
-40	-20.11	-20.13	-3.71	-3.73
-50	-21.65	-21.67	-4.81	-4.83
-60	-22.73	-22.75	-5.38	-5.39

not steep, the estimated σ^o values from the two methods are again comparable. While for $|\theta| \leq 10^o$ where the σ^o vs θ curve is steep, the second method based on Eq. (3-27) tends to give a lower σ^o value than the first method. At $\theta = 5^o$, the difference in σ^o estimates from the two methods could be as much as ~2 dB.

From these comparisons, it can be concluded that when the σ^o is steeply decreasing with θ, the second method of σ^o derivation tends to underestimate the σ^o values. This suggests that, for observation over a smooth quiet water surface, the σ^o values at small θ derived from the second method (which is used in most cases) may have to be modified.

5.3 A SAMPLE POWER SPECTRUM

One way to show the scatterometer receiver data output is to plot the signal power density as a function of frequency. Figures 5-1 and 5-2 gave samples of such plots for the fore and aft beam respectively. The data shown in these figures were obtained from a functional check flight over Lake Livingston, Texas, in June 1977. The average aircraft speed and altitude were 77 m/sec and 469 m respectively. It was rather windy and the water surface was not smooth during the flight. The power spectra in both of the figures were generated with a bandwidth of 50 Hz and an integration time of 6 sec.

Several features are apparent from the observation of these figures. First, the power spectra from both fore and aft beams are comparable

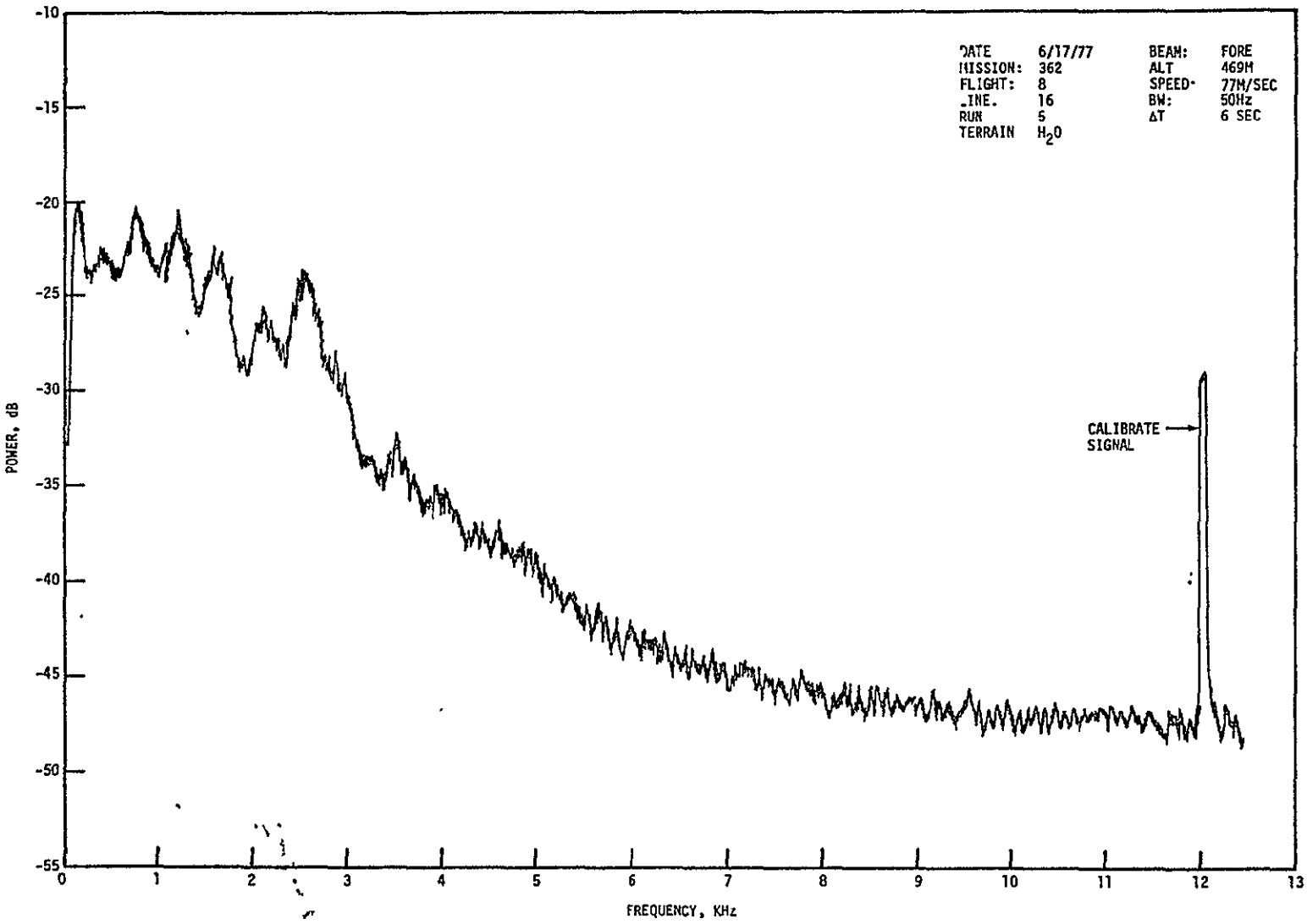

Figure 5-1.— A power spectrum plot of a 13 3 GHz scatterometer data set — fore beam, over water.

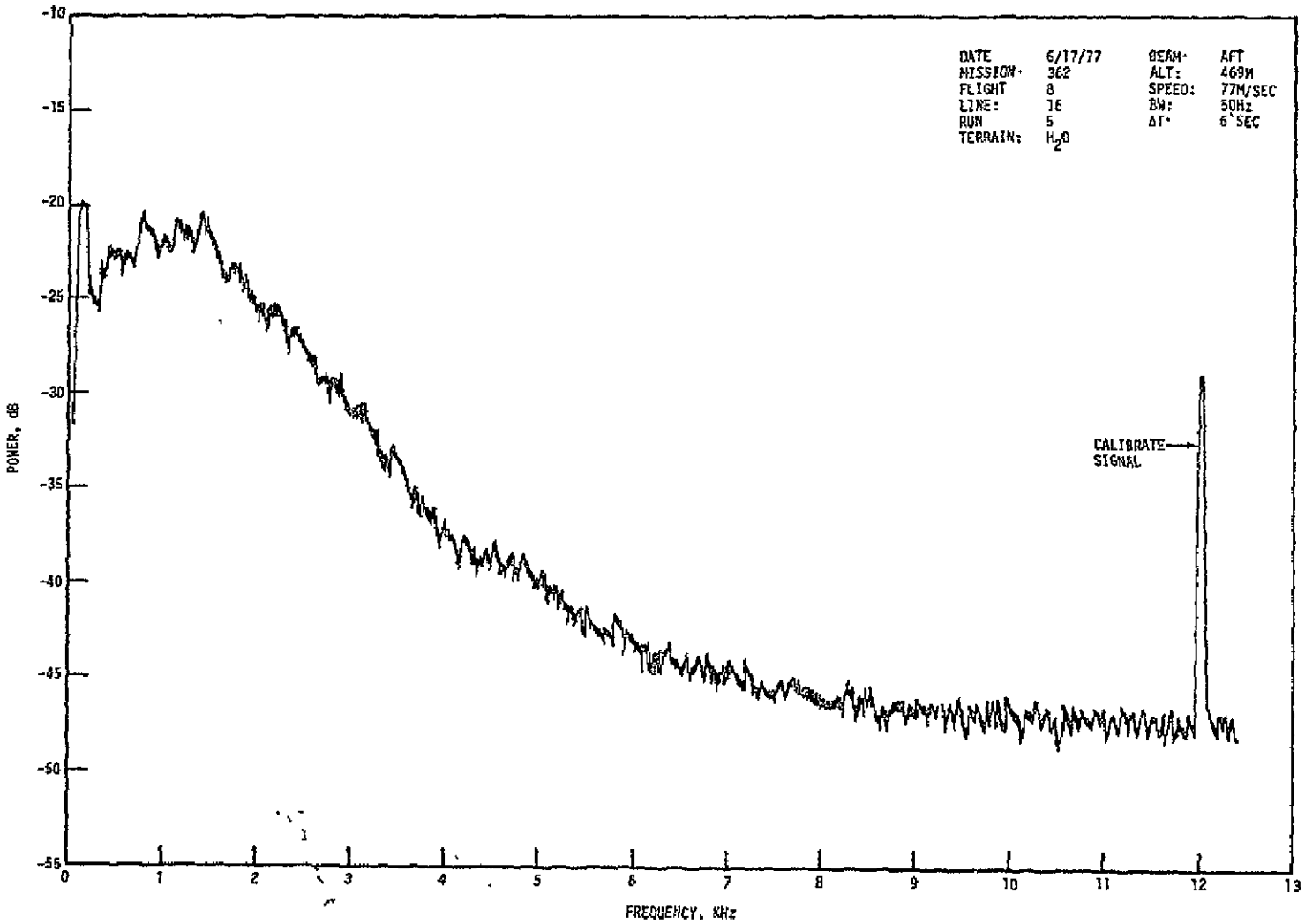

Figure 5-2.— A power spectrum plot of a 13.3 GHz scatterometer data set — aft beam, over water.

in general shapes and magnitudes. The noise floor was about ~-47 dB in both figures. Secondly, the fore-beam power spectrum showed several distinct ripples in the frequency range of interest <5 KHz. The aft-beam power spectrum in Figure 5-2, on the other hand, showed a reasonably smooth variation over the same frequency range. The difference in the fore - and the aft - beam power spectra could be due to the direction of the wind blow relative to the aircraft flight line. Thirdly, the signal clipping occurred at the frequency of ~150 Hz in both figures, although the water rolloff filters were used during the flight. Of course, the gain can be adjusted to avoid the signal clipping, but this can be done only at the expense of the small signal to noise ratio at large incident angles. The small dynamic range of the rolloff filters were previsouly noted in Section 3.

The backscattering coefficient σ^o could be estimated from Figures 5-1 and 5-2 at several selected incident angles θ. This was done using Eq. (3-27) and the results were plotted in Figure 5-3. The data obtained by Krishen (ref. 1) using the same scatterometer system was also included in the figure for comparison. The σ^o's derived from the fore and aft beams were comparable to within ~2 dB for most θ. They were also not too different from the data measured during a wind speed of ~25 knots (dashed curve). The σ^o values at $\theta \approx 50^o$ might not be good because of the small signal to noise ratio.

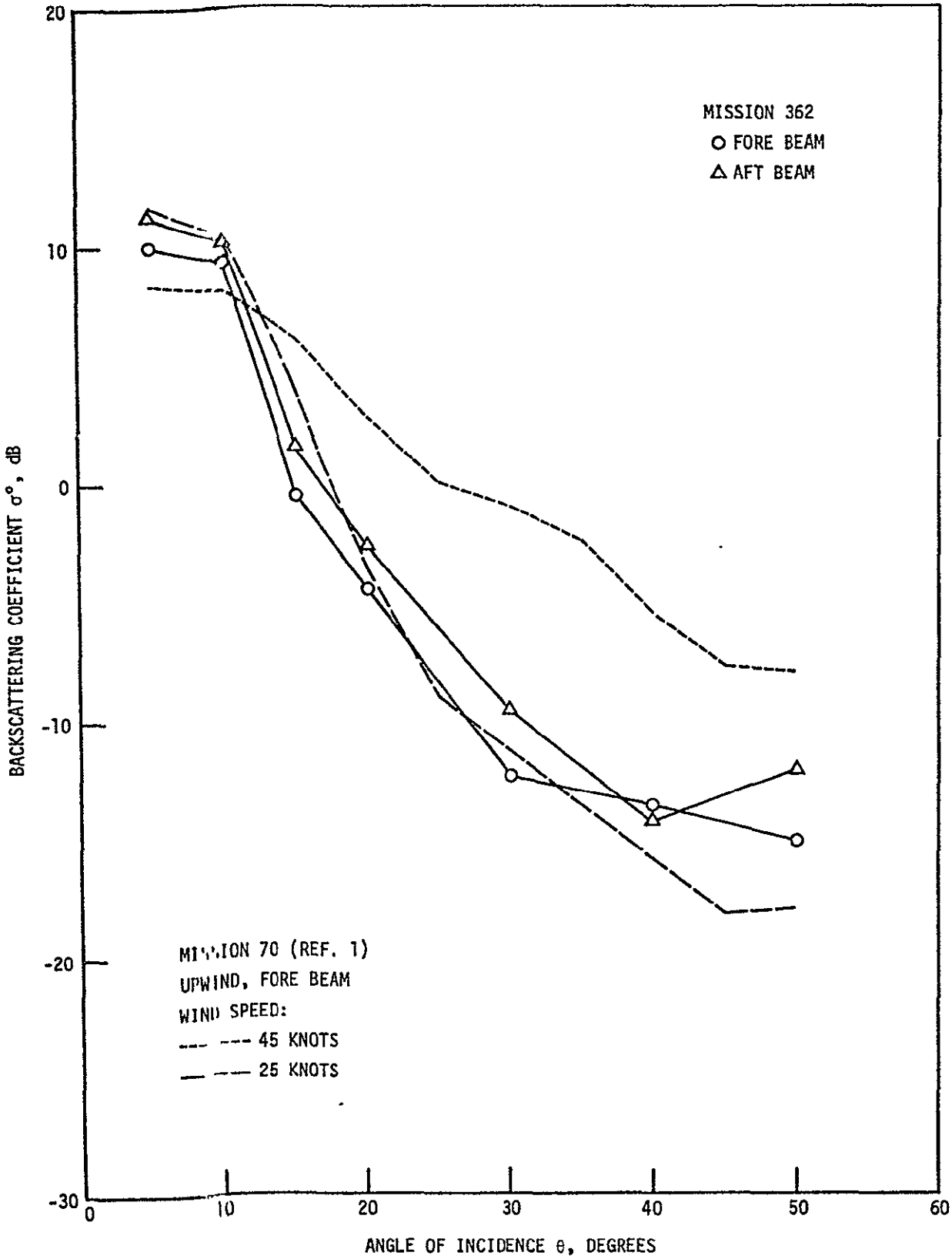

Figure 5-3.- A σ° vs. θ plot derived from figures 5-1 and 5-2.

5.4 PRECISION IN THE OUTPUT SIGNAL

The discussion in this section is limited to those factors directly related to the 13.3 GHz scatterometer system only. The backscattered signal statistics which were discussed in great length elsewhere (ref. 12) will not be repeated here. The following gives a brief description for each of these factors considered to affect the performance of the scatterometer system.

5.4.1 Antenna Pattern Measurements

The uncertainty in the antenna pattern measurements was not recorded and supplied together with the gain values. A reasonable estimate placed this measurement uncertainty at ~±0.5 dB (S. C. Reid, personal communication). An uncertainty of ~±0.5 dB in one-way gain results in the uncertainty of ~±0.7 dB for the two-way gain used in the σ^o estimates. Another possible source of uncertainty comes from the mounting of the antennae onto the aircraft. The antenna gain pattern was measured in a JSC laboratory. If care was not taken in the mounting of the antennae in the laboratory or in the aircraft, the laboratory coordinate system might not coincide with the aircraft coordinate system. As a result, a constant mounting bias might exist in the angle of incidence at which the gain was used in the σ^o estimates. The uncertainty from this source can not be easily assessed.

5.4.2 Measurements of Calibrate Constant and Rolloff Function

An uncertainty also exists in the measurements of the calibrate constant K and rolloff function $Z_w(f_d)$. A reasonable estimate

placed this uncertainty to be no more than ±0.5 dB for each of these measurements (S. C. Reid, personal communication).

5.4.3 Aircraft Parameters

Factors associated with aircraft motion such as roll, pitch, drift, vertical velocity, speed and altitude changes could introduce errors in the received signals. The effects of roll, pitch, and vertical velocity are to alter the incident angle θ. These effects were studied by Krishen et. al. (ref. 7) with respect to the same 13.3 GHz scatterometer system using the antenna pattern data measured in 1969. Following the same approach, the errors introduced by these factors in the σ^o derivation were estimated with respect to the newly measured antenna pattern data. The results were presented in Tables 5-3, 5-4, and 5-5. In making these error calculations, the aircraft speed is assumed to be 80 m/sec, the vertical velocity to be 4 m/sec, and both roll and pitch angles to be 5^o. Clearly, the change in θ due to pitch and vertical speed could be either plus or minus. The examples shown in Tables 5-4 and 5-5 consider the case of larger modified incident angles in the fore beam only (smaller modified incident angles in the aft beam). The roll angle also changes the distance R. The values shown in Table 5.3 also includes the effect of the distance change.

The changes of both aircraft speed and drift would introduce changes in the Doppler frequency associated with a given θ. For example, at $\theta = 30^o$, a change of speed from 80 m/sec to 75 m/sec would give a corresponding change in Doppler frequency from 3548 Hz

TABLE 5-3. - ERRORS INTRODUCED IN THE σ^o ESTIMATES DUE TO AN AIRCRAFT ROLL OF 5^o

Fore Beam			Aft Beam		
Angle of Incidence (Degree)	Modified Angle of Incidence (Degree)	Error in σ^o (dB)	Angle of Incidence (Degree)	Modified Angle of Incidence (Degree)	Error in σ^o (dB)
5	7.07	-0.9	-5	-7.07	-1.9
10	11.17	-0.2	-10	-11.17	0.2
15	15.79	0.6	-15	-15.79	0.1
20	20.59	0.2	-20	-20.59	0.1
30	30.38	-0.3	-30	-30.38	-0.4
40	40.26	0.1	-40	-40.26	-0.2
50	50.18	-0.2	-50	-50.18	-0.3
60	60.13	-0.1	-60	-60.13	-0.2

TABLE 5-4. - ERRORS INTRODUCED IN THE σ^{o} ESTIMATES DUE TO AN AIRCRAFT PITCH OF 5^{o}

Fore Beam			Aft Beam		
Angle of Incidence (Degree)	Modified Angle of Incidence (Degree)	Error in σ^{o} (dB)	Angle of Incidence (Degree)	Modified Angle of Incidence (Degree)	Error in σ^{o} (dB)
5	10	-3.3	-5	0	2.4
10	15	0.8	-10	-5	2.8
15	20	2.0	-15	-10	-2.4
20	25	0.4	-20	-15	-0.1
30	35	-3.5	-30	-25	3.1
40	45	-0.1	-40	-35	-1.5
50	55	-4.0	-50	-45	4.1
60	65	-3.5	-60	-55	2.4

TABLE 5-5. - ERRORS INTRODUCED IN THE σ^{o} ESTIMATES DUE TO AN AIRCRAFT VERTICAL SPEED OF 4 M/SEC.

Fore Beam			Aft Beam		
Angle of Incidence (Degree)	Modified Angle of Incidence (Degree)	Error in σ^{o} (dB)	Angle of Incidence (Degree)	Modified Angle of Incidence (Degree)	Error in σ^{o} (dB)
5	7.86	-1.1	-5	-7.86	-2.0
10	12.86	-0.3	-10	-12.86	1.1
15	17.86	1.5	-15	-17.86	0.1
20	22.86	0.1	-20	-22.86	0.8
30	32.86	-1.9	-30	-32.86	-2.1
40	42.86	1.0	-40	-42.86	-0.5
50	52.86	-2.2	-50	-52.86	-2.0
60	62.86	-1.4	-60	-62.86	-2.5

to 3326 Hz. Similarly, a drift of ~10° would shift the Doppler frequency from 3548 Hz to 3494 Hz. These changes in Doppler frequency, if not corrected for in data processing, could result in erroneous σ^o estimates.

The variation in aircraft altitude would also introduce error in the σ^o estimate. From Eq. (3-3), σ^o is observed to be proportional to R^4 and inversely proportional to the area A of the ground cell. Since R is proportional to altitude h and A to h^2, σ^o varies with h^2. Thus, if h changes from 460 m to 440 m, the error in the σ^o estimate would be ~0.39 dB.

5.4.4 Additional Error Sources

Several additional error sources should also be considered. The first source was discussed by Krishen et. al. (ref. 7) in great detail. The second source of error had its origin in the electronics assembly. Zusfeldt (ref. 14) analyzed such an error source in detail for the 1.6 GHz scatterometer system. It is expected that the same kind of error also exists in the 13.3 GHz system. However, the magnitude of this error source is small and is mostly taken care of by the system calibration in the laboratory. Finally, if σ^o vs. θ curve is steep, error could be present in σ^o estimate at small incident angles, as pointed out in Subsection 5.1.

5.4.5 A Brief Comment

If the mounting of the antennae in the laboratory gain measurements or in the aircraft should not be precise, then error would be

present in the σ^o estimates. Because of the existence of many ripples in the antenna gain factor variation with incident angle θ, this imprecise antenna mounting tends to create bumps in the σ^o vs. θ curve. As a result, the interpretation of the data with respect to the wave backscattering from terrain surface may turn out to be very difficult. Thus, the error in the antenna mounting should be kept as small as possible.

The calibrate signal level could be adjusted to accomodate a particular mission. For each adjustment a new calibrate constant K would have to be measured and the measurement, therefore, should be made as precise as possible. The changes in aircraft parameters could introduce large error in σ^o estimation. This type of error could be minimized by making corrections to the aircraft parameters during data processing. The error sources from the improper phase shift and the steepness of σ^o vs. θ curve could be reduced to a minimum by proper data reduction and manipulation. However, if the data quality is such that the ratio of the fore to aft signal powers is large or small compared to 1, a few degrees in phase shift error could result in large error in σ^o estimate. The data should be used with reservation in this case.

6. CONCLUSIONS AND RECOMMENDATIONS

A system analysis was performed for the JSC 13.3 GHz airborne scatterometer. The principle of the scatterometer operation, calibration procedures, and data handling were described in some detail. The antenna gain patterns were studied in great length and the effects of the antenna side lobes and cross polarization analyzed. Several error sources in the estimation of σ^o were briefly discussed. In the course of the entire analysis, only the immediate power input to and the power output from the scatterometer system were dealt with. The interacting process of the RF waves with terrain surface was completely omitted. The terrain surface characteristics were reflected through the assumed functional forms of the backscattering coefficient $\sigma^o(\theta)$.

The major conclusions that resulted from this study are listed in the following:

1. When σ^o decreases rapidly with incident angle θ, which occurs in the backscattering from a quiet water surface, the normal approach of estimating σ^o appears to give a low value at a small incident angle. If σ^o vs θ curve over water is given by Figure 3-4, then the amount of the underestimate is ~2 dB at $\theta = 5^o$.

2. The contributions to the receiver signal input due to the effect of the antenna side lobe gain and cross polarization

were examined in detail. These undesirable signal contributions were found to be negligible.

3. It was found that the rolloff filters of the 13.3 GHz scatterometer system did not cover enough dynamic range. Because of this lack in dynamic range, the signal power input at low frequencies (small incident angles) might saturate for observation over a smooth surface. If the gain was adjusted to avoid signal saturation, then the signal to noise ratio would deteriorate at high frequencies (large incident angles).

4. The method of antenna gain measurements for the 13.3 GHz scatterometer was found to be somewhat different from that for the 1.6 GHz scatterometer. As a result, the data processing equations for the two systems should differ also. To maintain the same processing equation for both systems, the measured antenna gain pattern of one system would have to be coordinate - transformed in conformation to the other.

5. Because of the rapid changes of the antenna gain factor with the angle of incidence, the variations of the aircraft parameters were found to strongly affect the estimation of σ^o. For example, a pitch of 5^o could produce as much as ~4 dB difference in σ^o estimate at some incident angles.

6. The antenna gain pattern in the fore beam was found to possess double maxima in the cross-track gain profile. This would present some difficulty in determining the antenna beamwidth with the 3-dB method.

There are five recommendations that are considered to be important in the improvements of the system performance and the quality of the final results. They are listed below:

1. For observations over a smooth surface where σ^o decreases rapidly with θ, care should be taken not to underestimate the σ^o values at small θ.

2. The sea rolloff filters in the 13.3 GHz scatterometer system have been utilized in both land and sea observations. It appears that the land rolloff filters are not of much use to the system. The sea rolloff filters alone do not have enough dynamic range to cover observations over both rough and smooth surfaces. Perhaps the land rolloff filters should be modified to improve the dynamic range of the entire system.

3. The mounting of the antennae onto the aircraft or in the laboratory for gain measurements should be done with extreme care to minimize error. A mounting error of 1^o could introduce ~1 dB error in σ^o estimates at some incident angles. Once the antennae were installed in the

aircraft, perhaps they should not be taken out again unless it was absolutely necessary to do so.

4. Although the operational principle is the same for both the 13.3 GHz and the 1.6 GHz scatterometers, the slight differences in the laboratory calibration (see Appendix A), in the antenna gain measurements, and in the location of the calibrate signals should be noted. These differences should be taken care of in the design and implementation of the data processing procedure to avoid errors.

5. Data acquired from the 13.3 GHz system should be checked with respect to the phase shift error. Corrections to the variations of the aircraft parameters should be made as precise as possible in the data processing.

7. REFERENCES

1. Krishen, K. : "Correlation of Radar Backscattering Cross Sections With Ocean Wave Height and Wind Velocity." J. Geophys. Res., Vol. 76, No. 27, PP 6528 - 6539, September 1971.

2. Bradley, G. A. : "Remote Sensing of Ocean Winds Using a Radar Scatterometer." University of Kansas/Center for Research, Inc. Technical Report 177-22, September 1971.

3. Rouse, J. W. : "Arctic Ice Type Identification by Radar." Proceedings of the IEEE, Vol. 57, No. 4, PP 605 - 611, April 1969

4. Parashar, S. K., Haralick, R. M., Moore, R. K., and Biggs, A. W. : "Radar Scatterometer Discrimination of Sea Ice Types." IEEE Transactions on Geoscience Electronics, Vol. GE-15, No. 2, PP 83 - 87, April 1977.

5. Dickey, F. M., King, C., Holtzman, J. C., and Moore, R. K. : Moisture Dependency of Radar Backscatter From Irrigated and Non-irrigated Fields at 400 MHz and 13.3 GHz."

6. Rouse, J. W., MacDonald, H. C., and Waite, W. P. : "Geoscience Applications of Radar Sensors."IEEE Transactions on Geoscience Electronics, Vol. GE-7, No. 1, PP 2 - 19, January 1969.

7. Krishen, K., Vlahos, N., Brandt, O., and Graybeal, G. : "Results of Scatterometer System Analysis for NASA/MSC Earth Observations Sensor Evaluation Program." Proceedings of the 7th International Symposium on Remote Sensing of Environment, The University of Michigan, Ann Arbor, Michigan, May 1971.

8. Rosenkranz, W. A. : "A Model of The 13.3 GHz Scatterometer." Lockheed Electronics Company, Inc., Technical Report LEC-8795, June 1976.

9. Reid, R. C. : "Joint Soil Moisture Experiment (JSME) Scatterometer Systems." Lockheed Electronics Company, Inc., Technical Report LEC-7195, October 1975.

10. "An Airborne Radar Scatterometer Signal Processing System." Texas A & M University Progress Report RSC 3182-1, February - April, 1975.

11. Wang, J. R. : "A Model of The 1.6 GHz Scatterometer." Lockheed Electronics Company, Inc., Technical Report LEC-10521, July 1977.

12. Manual of Remote Sensing - Microwave Remote Sensors, Chapter 9, American Society of Photogrammetry (Publisher), 1975.

13. Beauchamp, K. G. : "Signal Processing Using Analog and Digital Techniques." John Wiley & Sons, Inc., New York, 1973.

14. Zeufeldt, R. D. : "1.6 GHz Dual Polarized Scatterometer System." Scatterometer Data Analysis Final Report, Volume 5, Report No. 57667-5, Teledyne Rayn Aeronautical Company, August 1970.

15. Reid, S. C. : "Laboratory Calibration/Performance Test Procedure 13.3 GHz Single Polarized Scatterometer." Lockheed Electronics Company, Inc., Technical Report LEC-3695, June 1974.

16. Soohoo, R. F. : "Microwave Ferrite Materials and Devices." IEEE Transactions on Magnetics, Vol. MAG-4, No. 2, PP 118 - 133, June 1968.

17. Skolnik, M. I. : Radar Handbook, Chapter 5, McGraw-Hill Book Company, 1970.

APPENDIX A

THE CALIBRATION DATA

THE CALIBRATION DATA

The laboratory calibration procedure for the 13.3 GHz scatterometer was described in detail by Reid (ref. 15). Therefore, only the calibration results will be given in the following. The calibrate data presented here were obtained during August of 1976 and were used in all the calculations in this document. Updating of these data are necessary whenever a new calibration is made for a major mission.

A.1 THE CALIBRATE CONSTANT

As discussed in Section 3, the constant K which relates the transmit and receive signal levels to those actually recorded at the receiver output has to be predetermined in the laboratory. The input signal to the receiver for the calibration derives from a broad band noise diode. Following the procedure given by Reid (ref. 15), K was determined to be 125.6 dB. Although the calibration procedure is almost identical for the 13.3 GHz and 1.6 GHz scatterometers, there is a basic difference in the input sources used. While the broad band noise is used for the calibration of the 13.3 GHz system, the input source for calibrating the 1.6 GHz system comes from a single side-band modulator. Because of this difference, the K values should be used with care in the data processing.

A.2 VARIABLE GAIN RESPONSE TEST

The reason for this test was to verify that the changes in the output signal correspond to the changes in the variable gain amplifier settings. The test results were given in Table A-1. The gain difference ΔG was taken between any one of the outputs at X2, X5 and X10 gain settings and the output at X1 gain setting. It is clear that the outputs of both channels correctly respond to the changes of gain setting. For example, when the (voltage)

TABLE A-1. - THE RECEIVER OUTPUT RESPONSES TO THE VARIABLE GAIN AMPLIFIER SETTINGS

Gain Setting	Channel 1		Channel 2	
	Output (dB)	ΔG (dB)	Output (dB)	ΔG (dB)
X1	-9.5		-8.8	
X2	-3.5	+6.0	-2.8	+6/0
X5	+4.5	+14.0	+5.2	+14.0
X10	+10.5	+20.0	+11.2	+20.0

Amplifier gain is increased by 10 times, the output power is observed to increase by 20 dB as expected.

A.3 THE ROLLOFF FUNCTION

The measurements of the sea(water) and land filter response as a function of audio-frequency (rolloff functions) were similar to that of determining the constant K. The results of these measurements were summarized in Table A-2 for both land and sea filters. It is clear from this table that, for either land or sea filters, the frequency responses of the two receiver output channels are very similar. The average frequency responses of the two receiver channels for both land and sea filters were plotted in Figure 3-3. Only the sea rolloff function was used in the calculations of the receiver output signal levels, because the land rolloff filters were found not to give enough attenuation at low frequencies and were of little practical use.

A.4 THE RECEIVER NOISE FIGURE

The measurements of the receiver noise figure were made at the frequencies of 2, 4, 6, 8 and 10 KHz. The results were summarized in the following table.

TABLE A-3.- THE RECEIVER NOISE FIGURE

Frequency (KHz)	Channel 1 (dB)	Channel 2 (dB)
2	20.2	21.7
4	17.7	20.7
6	16.2	18.2
8	15.7	17.5
10	15.7	17.5

There is some differences in the noise figure between channel 1 and channel 2 as noted from the table.

TABLE A-2. - THE MEASURED RESPONSES (ROLLOFF FUNCTIONS) IN dB FOR THE 13.3 GHz SCATTEROMETER RECEIVER OUTPUTS

Test Frequency (KHz)	Channel 1		Channel 2	
	Land	Water	Land	Water
10	-0.2	-0.3	-0.2	-0.5
8	-0.4	-0.9	-0.3	-0.9
4	-0.6	-3.1	-0.5	-3.5
2	-1.0	-7.0	-1.1	-7.2
1	-1.6	-12.5	-1.3	-12.6
0.8	-2.1	-14.0	-1.5	-14.2
0.4	-4.1	-20.0	-4.0	-20.2
0.2	-7.9	-26.0	-8.0	-26.2
0.1	-12.9	-32.0	-13.0	-32.2
0.08	-13.6	-34.0	-14.5	-34.2
0.04	-19.6	-40.0	-20.5	-40.2

APPENDIX B

THE FERRITE MODULATOR

THE FERRITE MODULATOR

To derive the absolute value of the backscattering coefficient σ^o as a function of incident angle θ from the backscattered Doppler signal return, it is necessary to maintain a reference calibrate signal, proportional to the transmitted power, in the receiver output. The 13.3 GHz scatterometer system uses a ferrite modulator to provide the reference signal required in the data reduction. The method is to amplitude modulate a sample of the transmitter power by a calibrate signal at 12 KHz and pass the sidebands of the modulation through the receiver network along with the backscattered signal. The ferrite modulator was installed in the channel which was not phase shifted. The single side-band power of the modulator as a function of the applied coil voltage was measured at several frequencies. The results were shown in Figure B-1.

The ferrite modulator employs the Faraday rotation principle and operates as a variable attenuator attenuating the RF energy passing through the modulator (refs. 2 and 16). If the maximum value of the rotation δ_m is sufficiently small, the output electric field E_o from the modulator is given by (ref. 16).

$$E_o = \frac{E_i}{2} \left[J_o(\delta_m) + 2 J_1 (\delta_m) \sin\omega_c t \right] \sin\omega_o t \qquad \text{(B-1)}$$

where E_i is the input electric field amplitude at frequency ω_o, and ω_c is the (calibrate signal) frequency at which the modulator was driven by an audio oscillator. J_o and J_1 are the Bessel functions. For small δ_m, $J_1 << J_o$. Using different approach, Bradley (ref. 2) essentially arrived at the same relationship between the input and output voltages.

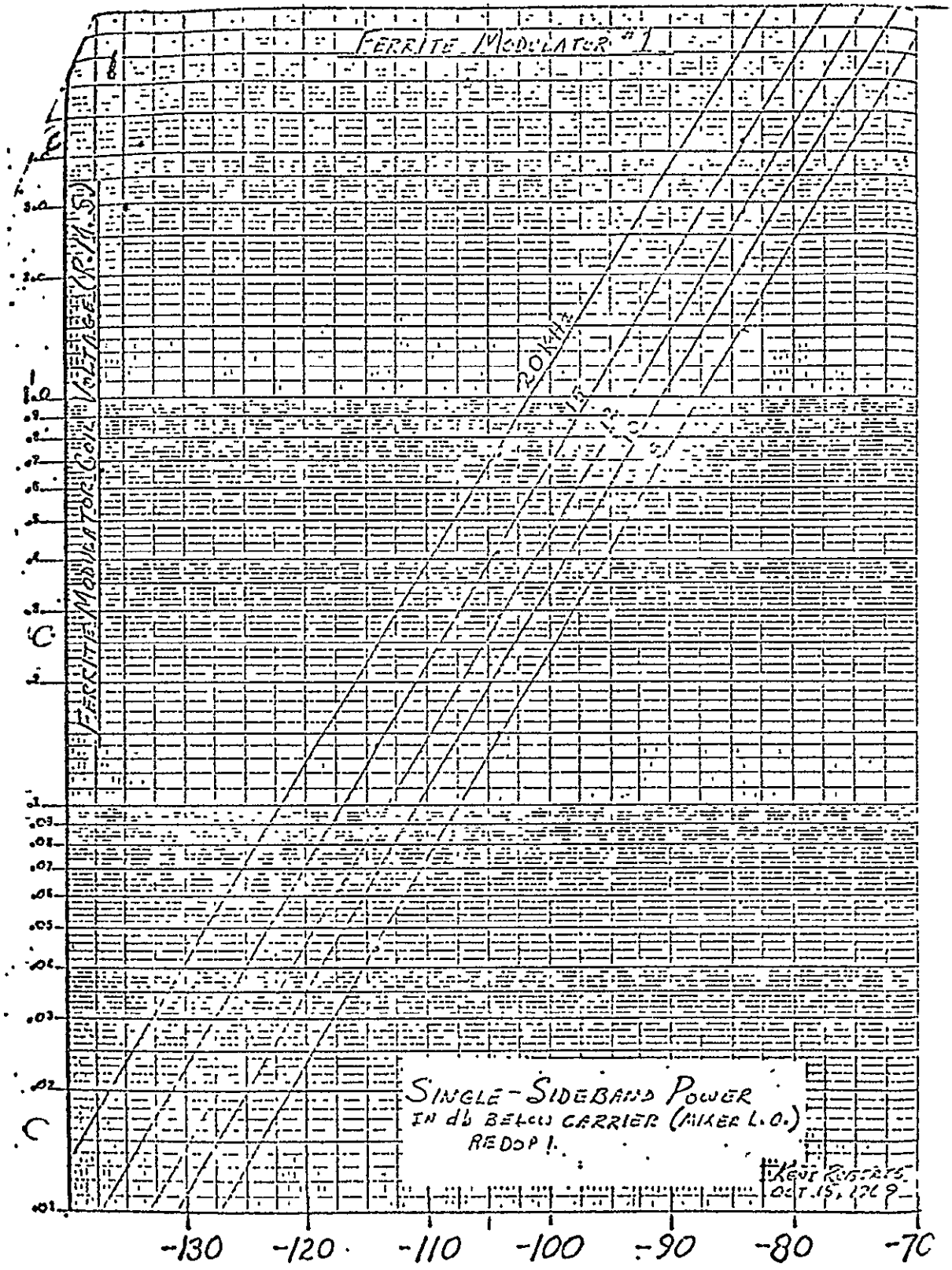

Figure B-1 -Ferrite modulator single sideband power

Thus the output voltage from the modulator can generally be written as:

$$V_{1F} = \alpha(1 + \gamma\cos\omega_c t)\ V_i \qquad \text{(B-2)}$$

Substituting Eq. (3-16a) for V_i, Eq. (B-2) becomes

$$V_{1F} = \frac{\alpha k_1}{2}\ (1 + \gamma\cos\omega_c t)\ \left\{ c_f \cos((\omega_o + \omega_d)\ t + X_f) + C_a \cos\ ((\omega_o - \omega_d)\ t + X_a) + \frac{2\rho_1 V_o}{k_1} \cos\omega_o t \right\}$$

$$= \frac{\alpha k_1}{2}\ \left\{ C_f \cos\ ((\omega_o - \omega_d)\ t + X_f) + C_A \cos\ ((\omega_o - \omega_d)\ t + X_a) + \frac{\rho_1 V_o \sqrt{2}}{k_1} \cos\omega_o t + \frac{\sqrt{2}\gamma\rho_1 V_o}{k_1} \cos\omega_o t \cos\omega_c t \right\} \qquad \text{(B-3)}$$

Two terms (product of calibrate and backscattered signals) inside the bracket in the above equation,

$$\gamma C_f \cos\omega_c t \cos((\omega_o t + \omega_d)\ t + X_f) \text{ and } \gamma C_a \cos\omega_c t \cos((\omega_o - \omega_d)\ t + X_a)$$

were omitted for the following reason. The ferrite modulator coil was generally operated at ~1.5 volts rms (S. C. Reid, personal communication). From Figure B-1, the single sideband power was found to be ~-90 dB below the power level of the local oscillator, i.e.,

$$20 \log \alpha\gamma = -90 \text{ dB} \qquad \text{(B-4)}$$

Now the range of backscattered signal power at receiver input was from ~-80 dBm to ~-120 dBm depending on the incident angles. The product of the signal return power would be ~-170 dBm to ~-210 dBm which were way below the noise floor of ~-139 dBm given in Table 2-3. Therefore, those two terms can be neglected and Eq. (B-3) represents the signal input to the mixer in Channel 1.

APPENDIX C

THE MIXER MATHEMATICAL MODEL

THE MIXER MATHEMATICAL MODEL

A mixer is essentially a nonlinear resistive element which combines the input signal with the local oscillator signal (the transmitter sample signal in the present case) and outputs signals at frequencies harmonically related to the input and local oxcillator frequencies and their mixtures. The characteristics of the nonlinear resistance for a typical mixer is shown in Figure C-1. One of the terms in Eq. (B-3) can be regarded as the local oscillator signal:

$$S_T(t) = \alpha\rho_1 V_o \cos {}_o t \qquad \text{(C-1)}$$

The remaining terms of Eq. (B-3) belong to $S_c(t)$.

Now the power series representation of the current I_{lm} flowing in the mixer may be expressed in terms of the voltage across the mixer terminals (ref. 17) as:

$$I_{lm} = a_o + a_1 V + a_2 V^2 + a_3 V^3 \ . \ . \ . + a_n V^n \qquad \text{(C-2)}$$

with

$$V(t) = S_T(t) + S_c(t)$$

The coefficient a generally decreases rapidly with n. Neglecting terms with $n \geq 3$, Eq. (C-2) becomes:

$$I_{lm} = a_o + a_1 (S_T + S_c) + a_2 (S_T + S_c)^2 \qquad \text{(C-3)}$$

By substituting the expressions for S_c and S_T, it is found that the signal given by Eq. (C-3) consists of DC terms as well as terms at the frequencies of ω_d, ω_c, $\omega_o \pm\omega_d$, ω_o, $\omega_o \pm\omega_c$, $2\omega_o$, $2\omega_c$, $2\omega_d$, $\omega_c \pm\omega_d$, $2\omega_o \pm\omega_d$, $2\omega_o \pm\omega_c$, $2\omega_o \pm 2\omega_d$, $2\omega_o \pm 2\omega_c$, $2\omega_o + \omega_d \pm\omega_c$, and $2\omega_o - \omega_d \pm\omega_c$. For the scatterometer system under study, ω_o = 13.3 GHz, ω_c = 12 KHz and $\omega_d \leq$ 9 KHz for aircraft speed < 200 knots.

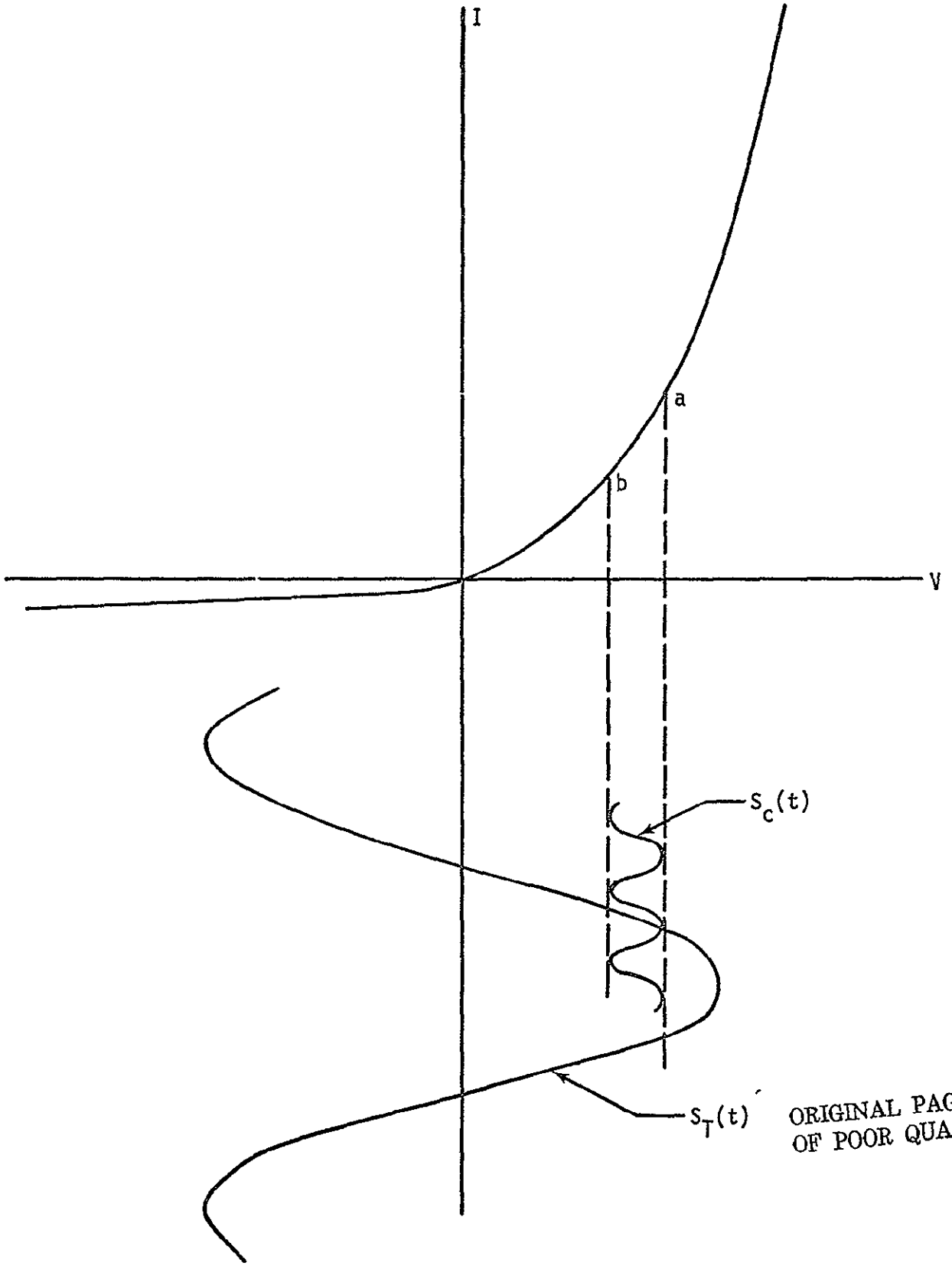

Figure C-1.— Characteristics of a nonlinear resistive element.

During the subsequent amplifier stages all the terms at the frequencies > 12 KHz are filtered out. Therefore, by retaining only the terms (except DC terms) at the frequencies < ω_c, the output signal voltage across the mixer load resistor R, is:

$$V_{lm} = \frac{R_l a_2 k_l}{2} \left\{ \alpha^2 C_f \rho_l V_o \cos(\omega_d t + X_f) + \alpha^2 C_a \rho_l V_o \cos(\omega_d t - X_a) \right.$$

$$+ \alpha^2 C_f \gamma \rho_l V_o \cos((\omega_c - \omega_d) t - X_f) + \cos((\omega_c + \omega_d) t + X_f)$$

$$+ \alpha^2 C_a \gamma \rho_l V_o \cos((\omega_c - \omega_d) t - X_a) + \cos((\omega_c + \omega_d) t + X_a)$$

$$\left. + \alpha^2 C_f C_a \cos(2\alpha_d t + X_f - X_a) t + \frac{2\alpha^2 \gamma \rho_l^2 V_o^2}{k_l} \cos {}_c t \right\} \quad \text{(C-4)}$$

The first, second, and last terms in Eq. (C-4) are the dominant terms. The power level of the local oscillator signal $\rho_l V_o \cos\omega_o t$ is only about ~36 dB below the transmitted power (Figure 2-2), which is much larger than the backscattered signal at ~460 m aircraft altitude. During calibration, the power level of the calibrate signal at frequency ω_c was set to be comparable to the backscattered signal, i.e., $\alpha^2 \gamma \rho_l^2 V_o^2 \sim \alpha^2 C_f \rho_l V_o$ or $\gamma \rho_l V_o \sim C_f$ (or $\gamma \rho_l V_o \sim C_a$, which also suggests that $\gamma << 1$). The ratio of the signal at frequency $\omega_c \pm \omega_d$ to that at ω_d is:

$$\frac{\alpha C_f \gamma \rho_l V_o}{2\alpha C_f \rho_l V_o} = \frac{\gamma}{2} << 1 \quad \text{(C-5)}$$

and the ratio of the signal at frequency $2\omega_d$ to that at ω_d is:

$$\frac{\alpha C_f C_a}{\alpha C_f \rho_l V_o} = \frac{C_a}{\rho_l V_o} \gamma << 1 \quad \text{(C-6)}$$

Thus the signals at frequencies $2\omega_d$ and $\omega_c \pm \omega_d$ can be neglected and Eq. (C-4) becomes:

$$V_{1m} = \frac{\beta_1 k_1 \rho_1 V_o}{2} \left\{ C_f \cos(\omega_d t + X_f) + C_a \cos(\omega_d t - X_a) + \frac{2\gamma\rho_1 V_o}{k_1} \cos\omega_c t \right\} \quad \text{(C-7)}$$

with $\beta_1 = \alpha^2 \alpha_2 R_1$. Following the same approach, it can be easily shown that the signal voltage output from the mixer in channel 2 is:

$$V_{2m} = \frac{\beta_2 k_2 \rho_2 V_o}{2} \left\{ -C_f \sin(\omega_d t + X_f) + C_a \sin(\omega_d t - X_a) \right\} \quad \text{(C-8)}$$

APPENDIX D

THE COMPUTER PROGRAM FLOW CHART AND LISTING

THE COMPUTER PROGRAM FLOW CHART AND LISTING

In order to calculate the receiver signal output according to Eq. (3-26), the incident angle θ_i, the distance R_i, and the area element ΔA_i, as shown in Figure D-1, should be expressed in terms of the measured quantities such as along-track incident angle $_o$, cross-track angle ϕ, altitude h and the along-track cell length ℓ. As mentioned before, the antenna measurements were made with a conical cut around the X' axis. In spherical coordinate system, X' - axis becomes the polar axis. And the polar angle is $90^o - \phi$ and the aximuthal angle is θ_o measured in the YZ plane. In this coordinate system the center of the area element ΔA_i is located at

$$X_i = h \sec\theta_{ip} \tan\phi_i$$

$$Y_i = h \tan \theta_{ip}$$

$$Z_i = h$$

The Doppler's relation gives:

$$\frac{2V}{\lambda} \sin\theta_o = \frac{2V}{\lambda} \frac{Y_i}{(X_i^2 + Y_i^2 + Z_i^2)^{\frac{1}{2}}}$$

or

$$\sin\theta_o = \frac{\tan\theta_{ip}}{(\sec^2\theta_{ip} \tan^2\phi_i + \tan^2\theta_{ip} + 1)^{\frac{1}{2}}}$$

$$\sin\theta_{ip} = \sin\theta_o \sec\phi_i \qquad \text{(D-1)}$$

The distance R_i, with the help of Eq. (D-1), is given by

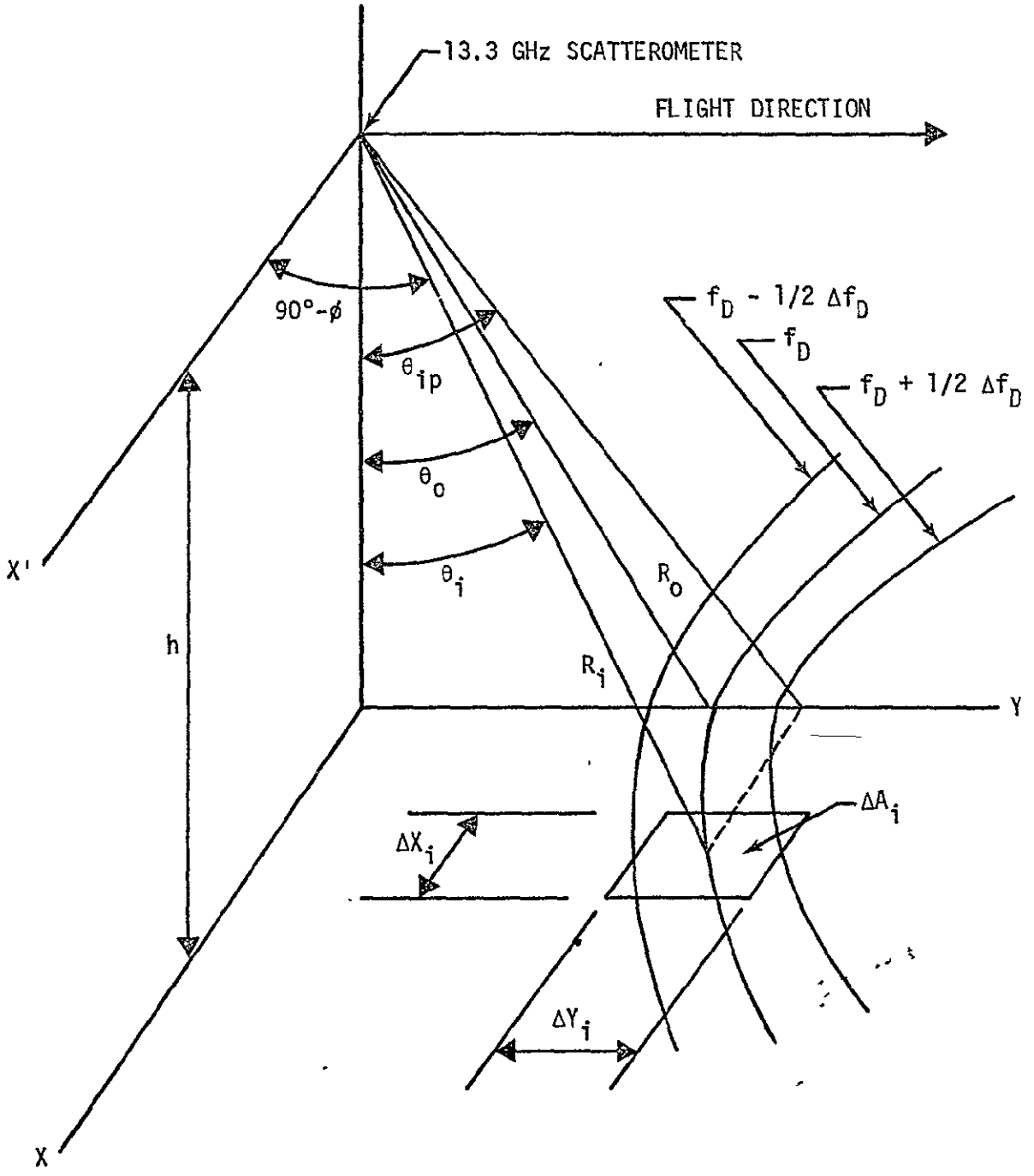

Figure D-1.— The geometry of an area element used in the numerical integration.

$$R_i = h \sec\theta_{ip} \sec\phi_i = \frac{h}{(\cos^2\phi_i - \sin^2\theta_o)^{\frac{1}{2}}} \qquad \text{(D-2)}$$

The angle of incidence θ_i needed in obtaining α^o value for numerical calculation is

$$\theta_i = \cos^{-1} \frac{h}{Ri} = \cos^{-1} (\cos^2\phi_i - \sin^2\theta_o)^{\frac{1}{2}} \qquad \text{(D-3)}$$

The area element is given by

$$\Delta A_i = \Delta X_i \, \Delta Y_i \qquad \text{(D-4)}$$

with

$$\Delta X_i = X_{i2} - X_{i1} = h \left\{ \frac{\sin\phi_{i2}}{(\cos^2\phi_{i2} - \sin^2\theta_o)^{\frac{1}{2}}} - \frac{\sin\phi_{i1}}{(\cos^2\phi_{i1} - \sin\theta_o)^{\frac{1}{2}}} \right\} \qquad \text{(D-5)}$$

and

$$\Delta Y_i = \frac{\ell\cos\theta_o}{(\cos^2\phi_i - \sin^2\theta_o)^{\frac{1}{2}}} \qquad \text{(D-6)}$$

The angles ϕ_{i1} and ϕ_{i2} are related to ϕ_i (all units in degrees) by

$$\phi_{i1} = \phi_i - 0.5 \qquad \text{(D-7)}$$

$$\phi_{i2} = \phi_i + 0.5 \qquad \text{(D-8)}$$

The above expression for R_i, θ_i, and ΔA_i were used in the computer program for calculating the receiver signal output.

The flow charts of the main program and the subroutine GAAT are displayed in Figures D-2 and D-3 respectively. The listing of the whole program is given in Table D-1. Three subroutines RINIT, RWRITE, and RREAD are used to initialize, to write data into, and

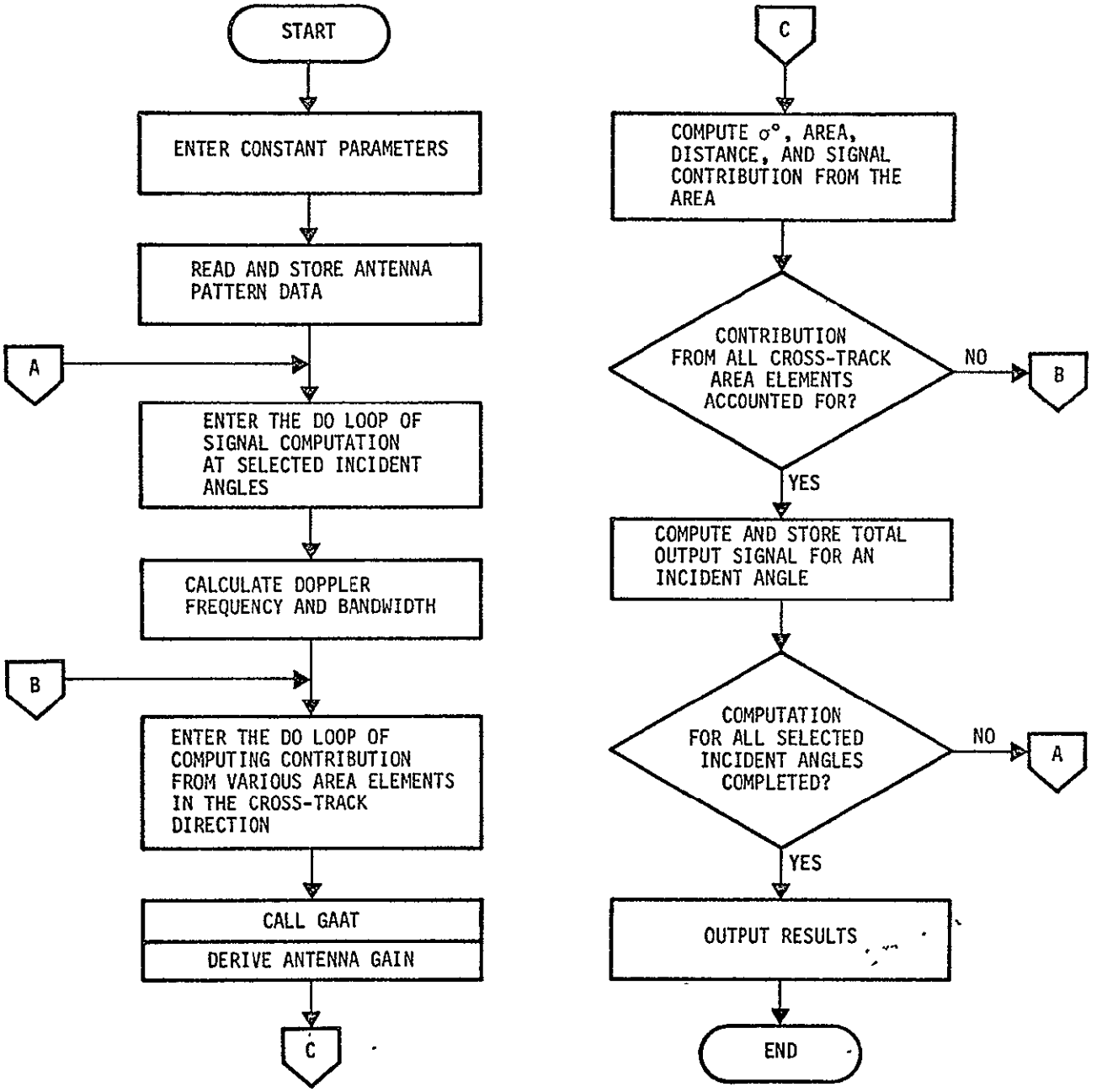

Figure D-2.— The MAIN program flow chart.

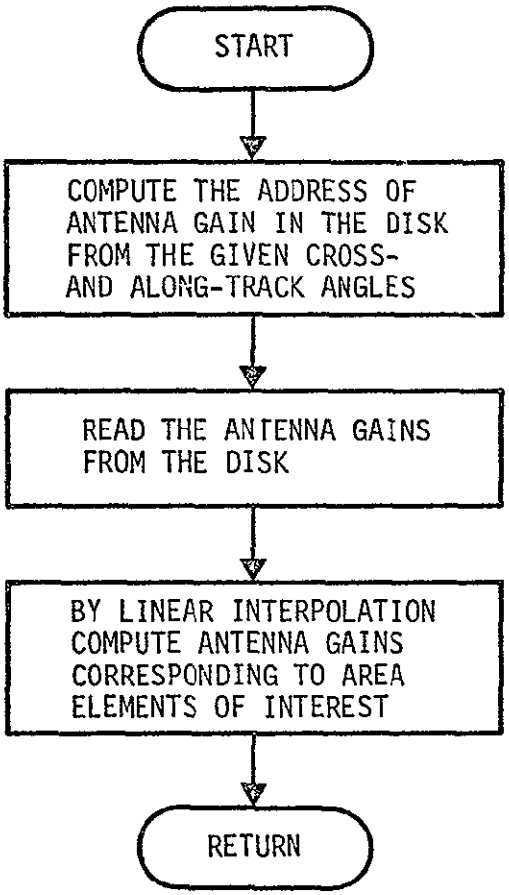

Figure D-3.- Subroutine GAAT flow chart.

TABLE D-1.-THE COMPUTER PROGRAM LISTING

```
 1*              DIMENSION THETA(8),POW(16),ROFF(8),BUF(181)
 2*              DATA THETA/5.,10.,15.,20.,30.,40.,50.,60./
 3*              DATA ROFF/16.6,10.8,7.8,6.0,4.0,2.9,2.2,1.8/
 4*              COMMON/B/IDADD,IX,IY,IXMAX,IYMAX
 5*        C ENTER CONSTANT PARAMETERS.
 6*              PIE=3.1416
 7*              HA=46.
 8*              VA=60.
 9*              SLAMD=0.02255
10*              CELEN=25.
11*              PI=PIE/180.
12*              SCAL=125.6
13*        C GET DISC AREA
14*              CALL RINIT(IDADD,NWRDS)
15*              K=IDADD
16*              READ(1)IYMAX,IXMAX,DB1,DB2,DPMAX
17*              IX=(IXMAX*2.)+1
18*              IY=(IYMAX*2.)+1
19*        C PUT ANTENNA GAINS ON DISC.
20*              DO 100 I=1,IY
21*              READ(1)N,BUF
22*              WRITE(6,4000)(BUF(K),K=1,IX)
23*              CALL RWRITE(K,BUF,IX,NSTAT)
24*         5    IF(NSTAT.EQ.1)GO TO 5
25*              IF(NSTAT.NE.0)WRITE(6,7000)N
26*              K=K+IX
27*        100   CONTINUE
28*        C ENTER MAIN LOOP OF COMPUTATION.
29*        C POWER COMPUTATION FOR EACH INCIDENT ANGLE.
30*              DO 500 I=1,8
31*              THTA=THETA(I)*PI
32*              FDOP=2.*VA*SIN(THTA)/SLAMD
33*              DF=2.*VA*(COS(THTA)**3)*CELEN/HA/SLAMD
34*              CLAMD=SLAMD**2
35*              CPI=(4.*PIE)**3
36*              SUMF=0.
37*              SUMA=0.
38*        C CROSS TRACK COMPUTATION.
39*              DO 400 J=1,7
40*              PHI=(J-1)*PI
41*              PHIL=((J-1)-0.5)*PI
42*              PHIR=((J-1)+0.5)*PI
43*              FAC=SQRT((COS(PHIR)**2)-(SIN(THTA)**2))
44*              XPHR=SIN(PHIR)/FAC
45*              XPHL=SIN(PHIL)/FAC
46*              DX=HA*(XPHR-XPHL)
47*              DY=CELEN*COS(THTA)/FAC
48*              DA=DX*DY
49*              R=HA/FAC
50*              RR=R**4.
51*              THINC=ACOS(FAC)
52*              THINC=THINC/PI
53*              SIGMA=(163.2/(THINC**0.76))-30.
54*              AI=ASIN(SIN(THTA)/COS(PHI))
55*              AI=AI/PI
56*              CALL GAAT(FGL,FGR,AGL,AGR,J,AI)
57*              SIG=10.**(SIGMA/10.)
58*              SUMA=SUMA+((AGL+AGR)*SIG*DA/RR)
59*              SUMF=SUMF+((FGL+FGR)*SIG*DA/RR)
60*              WRITE(6,6000)FGL,FGR,AGL,AGR,SUMF,SUMA,SIGMA,DA,RR
61*        400   CONTINUE
62*        C CALCULATE POWER OUTPUT FOR AN INCIDENT ANGLE.
```

TABLE D-1.- Continued

```
 63*                FPAC=SUMF*CLAMD/CPI/DF
 64*                APAC=SUMA*CLAMD/CPI/DF
 65*                FPAC=10.*ALOG10(FPAC)
 66*                APAC=10.*ALOG10(APAC)
 67*                WRITE(6,6000)FPAC,APAC,FDOP,DF,CLAMD,CPI,SCAL,DX,DY
 68*                POW(I)=FPAC-POFF(I)+SCAL
 69*                POW(I+8)=APAC-POFF(I)+SCAL
 70*      500       CONTINUE
 71*                WRITE(6,1000)
 72*                WRITE(6,2000)(POW(I),I=1,8)
 73*                WRITE(6,3000)
 74*                WRITE(6,2000)(POW(I),I=9,16)
 75*                STOP
 76*     1000       FORMAT(2H ,'INCIDENT ANGLE AT',3X,'5',11X,'10',10X,'15',
 77*           11HX,'20',10X,'30',10X,'40',10X,'50',10X,'60',//)
 78*     2000 FORMAT(16X,8F12.4)
 79*     3000       FORMAT(2H ,'INCIDENT ANGLE AT',2X,'-5',10X,'-10',9X,'-15',
 80*           19X,'-20',9X,'-30',9X,'-40',9X,'-50',9X,'-60',//)
 81*     4000       FORMAT(20F6.1)
 82*     6000       FORMAT(9013.4)
 83*     7000       FORMAT(2H ,'TAPE PROBLEM AT ANGLE',I5)
 84*                END
```

```
  1*                SUBROUTINE GAAT(FGL,FGR,AGL,AGR,J,AI)
  2*                COMMON/B/IDADD,IX,IY,IXMAX,IYMAX
  3*                DIMENSION ABUF1(181),ABUF2(181),FBUF1(181),FBUF2(181)
  4*      C DETERMINE THE POSITIONS OF THE ANTENNA FOOTPRINTS
  5*                IR=IXMAX
  6*                IL=IXMAX+2
  7*                IM=IXMAX+1
  8*                IA=AINT(AI)
  9*                IAPP=IA+1
 10*                IAF1=IYMAX+IA
 11*                IAA1=IYMAX-IA
 12*                IAF2=IAF1+1
 13*                IAA2=IAA1-1
 14*                IAP1=IAA1*IX+IDADD
 15*                IAP2=IAA2*IX+IDADD
 16*                IFP1=IAF1*IX+IDADD
 17*                IFP2=IAF2*IX+IDADD
 18*      C READ    ANTENNA RECORDS
 19*                CALL RREAD(IAP1,ABUF1,IX,IST)
 20*           5    IF(IST.EQ.1)GO TO 5
 21*                IF(IST.NE.0)WRITE(6,1000)IA
 22*                CALL RREAD(IAP2,ABUF2,IX,IST)
 23*           6    IF(IST.EQ.1)GO TO 6
 24*                IF(IST.NE.0)WRITE(6,1000)IAP1
 25*                CALL RREAD(IFP1,FBUF1,IX,IST)
 26*           7    IF(IST.EQ.1)GO TO 7
 27*                IF(IST.NE.0)WRITE(6,1000)IA
 28*                CALL RREAD(IFP2,FBUF2,IX,IST)
 29*           8    IF(IST.EQ.1)GO TO 8
 30*                IF(IST.NE.0)WRITE(6,1000)IAP1
```

TABLE D-1.- Continued

```
      WRITE(6,2000)(ABUF1(K),K=1,IX)
      WRITE(6,2000)(ABUF2(K),K=1,IX)
      WRITE(6,2000)(FBUF1(K),K=1,IX)
      WRITE(6,2000)(FBUF2(K),K=1,IX)
C OBTAIN THE ANTENNA GAIN VALUES
      IF(J.EQ.1)GO TO 10
C AFT BEAM ANTENNA GAIN
      APL1=ABUF1(IL-J)
      APL2=ABUF2(IL-J)
      APR1=ABUF1(IR+J)
      APR2=ABUF2(IR+J)
      APL1L=10.**(APL1/10.)
      APL2L=10.**(APL2/10.)
      APR1L=10.**(APR1/10.)
      APR2L=10.**(APR2/10.)
C FORE BEAM ANTENNA GAIN
      FPL1=FBUF1(IL-J)
      FPL2=FBUF2(IL-J)
      FPR1=FBUF1(IR+J)
      FPR2=FBUF2(IR+J)
      FPL1L=10.**(FPL1/10.)
      FPL2L=10.**(FPL2/10.)
      FPR1L=10.**(FPR1/10.)
      FPR2L=10.**(FPR2/10.)
C LINEAR INTERPOLATION.
      AGL=(((AI-IA)/(IAPP-IA))*(APL2L-APL1L))+APL1L
      AGR=(((AI-IA)/(IAPP-IA))*(APR2L-APR1L))+APR1L
      FGL=(((AI-IA)/(IAPP-IA))*(FPL2L-FPL1L))+FPL1L
      FGR=(((AI-IA)/(IAPP-IA))*(FPR2L-FPR1L))+FPR1L
      GO TO 15
   10 CONTINUE
C AFT BEAM ANTENNA GAIN, ALONG TRACK
      AP1=ABUF1(IM)
      AP2=ABUF2(IM)
      AP1=10.**(AP1/10.)
      AP2=10.**(AP2/10.)
C FORE BEAM ANTENNA GAIN, ALONG TRACK
      FP1=FBUF1(IM)
      FP2=FBUF2(IM)
      FP1=10.**(FP1/10.)
      FP2=10.**(FP2/10.)
C LINEAR INTERPOLATION.
      AGL=(((AI-IA)/(IAPP-IA))*(AP2-AP1))+AP1
      AGR=0.
      FGL=(((AI-IA)/(IAPP-IA))*(FP2-FP1))+FP1
      FGR=0.
   15 CONTINUE
      WRITE(6,4000)AGL,AGR,FGL,FGR,AP1,AP2,FP1,FP2,AI,IA,J
      RETURN
 1000 FORMAT(1H ,'DISC READ PROBLEM FOR ANGLE',I5)
 2000 FORMAT(20F6.1)
 4000 FORMAT(1H ,9F8.2,2I10)
      END
```

to read data out of the high speed drum storage. These subroutines are stored in the local computer program library and explained in the JSC CAD Procedure Manual, Exec 8 System General User Information.